Sand-Mud Tidal Flat Morphodynamics Influenced by Alongshore Tidal Currents

Wang, Yunwei; Wang, Yaping; Yu, Qian; Du, Zhiyun; Wang, Zhengbing ; Gao, Shu

DOI
10.1029/2018JC014550

Publication date
2019

Document Version
Accepted author manuscript

Published in
Journal Of Geophysical Research-Oceans

Sand-Mud Tidal Flat Morphodynamics Influenced by Alongshore Tidal Currents

Yunwei Wang[1], Ya Ping Wang[2], Qian Yu[3*], Zhiyun Du[3], Zheng Bing Wang[4, 5], Shu Gao[2]

[1] Jiangsu Key Laboratory of Coast Ocean Resources Development and Environment Security, Hohai University, Nanjing, China.

[2] State Key Laboratory for Estuarine and Coastal Studies, East China Normal University, Shanghai, China.

[3] MOE Key Laboratory for Coast and Island Development, Nanjing University, Nanjing, China.

[4] Faculty of Civil Engineering and Geosciences, Delft University of Technology, Delft, the Netherlands.

[5] Deltares, Delft, the Netherlands.

Corresponding author: Q. Yu (qianyu.nju@gmail.com)

Key Points:

- Alongshore tidal currents play an important role in cross-shore morphodynamics and sediment zonation of tidal flats
- Strong alongshore currents transport sand landward from sub-tidal flat, resulting in sandy lower flat
- The upper flat is muddy and convex-up, dominated by cross-shore tidal currents

Abstract

Tidal flats, where significant land-ocean interactions take place, are often abstracted as a cross-shore bed profile with sediment zonation from the lower sand flat to the upper mud flat. However, in addition to cross-shore tidal currents, the impact of the alongshore components on cross-shore sediment transport, morphological evolution, and sediment grain-size change remains unclear. Here we investigated the sand-mud tidal flat morphodynamics in the absence of waves by combining approaches of field observations, numerical modeling, and analytical interpretations, based on the example of the tidal flat at the central Jiangsu coast, China. The results show that the morphodynamic processes are complicated by the interactions of cross-shore and alongshore tidal currents, cross-shore flat morphology, and sediment zonation. With identical tidal ranges and increased background alongshore tidal level phase lag, the alongshore currents gradually become dominant at the lower flat, while the upper flat is always dominated by the cross-shore currents. Therefore, in case of different alongshore tidal currents, tidally-dominated bed profiles at the upper flats are quite similar, being convex-up and consist of mud. In contrast, the strong alongshore currents can erode the mud at the lower flat, and promote the landward sand transport from the sub-tidal area to the lower flat, forming a sand flat. The tidally maximum bed shear stress is almost spatially uniform at the muddy area but pronouncedly elevated when the bed sediment coarsens at the lower flat. The contributions of the alongshore tidal currents and sand-mud sorting processes should be adequately addressed in similar coastal environments.

Plain language summary

Taken the example of the tidal flat at the central Jiangsu coast, China, we investigated the sand-mud tidal flat morphodynamics by field observations, numerical modeling, and analytical interpretations. We found that the cross- and alongshore tidal currents, cross-shore bed profiles, and sediment zonation interact as a complicated system, in which alongshore tidal currents play an important role in cross-shore morphodynamics. Strong alongshore currents transport sand landward from sub-tidal flat, forming a sandy lower flat, and the tidally maximum bed shear stress becomes much larger than at the muddy upper flat. So we can improve our understanding of the sediment dynamics and morphological evolution of tidal flats under the influence of alongshore tidal currents.

1 Introduction

Tidal flats, the transition between subaerial and submarine environments, are areas of significant land-ocean interactions (Flemming, 2003). They play an important role in material circulation, coastal protection and ecological conservation (Reise, 2001; Temmerman et al., 2013). With the accelerated influences of sea-level rise and human activities (e.g. land reclamation, harbor construction), the studies of tidal flat morphodynamics are crucial to making comprehensive coastal management strategies (French, 1997; Mangor et al., 2017). Based on previous observational and modeling works on the tidal flat sediment dynamics (Bartholdy & Kvale, 2006; Dyer, 2000; Fan, 2012; Flemming & Bartholomä, 1995; Nittrouer et al., 2013), this study focuses on the alongshore tidal currents impacts on the tidal flat morphodynamics with emphasis on the sand-mud sorting processes.

Cross-shore tidal currents being the main shaping factor, tidal flats are often abstracted as a one-dimensional cross-shore model in researches on their morphological and sedimentary characters (Hu et al., 2015; Kirby, 2000; Mariotti & Fagherazzi, 2010; Roberts et al., 2000; Pritchard & Hogg, 2003; Pritchard et al., 2002). The analytical solutions for equilibrium cross-shore tidal flat profiles were given by Friedrichs and Aubrey (1996), using the concept of spatially uniform maximum bed shear stress. The landward residual mud transport and the consequent cross-shore muddy profile progradation are attributed to spatial and local asymmetries (Friedrichs, 2011; Hsu et al., 2013; Maan et al., 2015).

However, in a number of field settings, the importance of alongshore tidal currents and related sediment transport processes (Figure 1) were also highlighted (Anderson, 1973; Collins et al., 1981; Gao, 2009a; Le Hir et al., 2000; Quaresma et al., 2007; Wang et al., 2006; Yang et al., 2003; Yu et al., 2017; Zhang, 1992). Thus, a quantitative framework is required on the impact of the alongshore tidal currents on tidal flat hydrodynamics, sediment transport, sediment grain size and bed level profiles, as well as their feedbacks to the alongshore currents.

Tidal flats have a general zonation in sedimentation that the surface sediment gradually changes from sand at the lower flat to mud at the upper flat (Figure 1) (Amos, 1995; Gao, 2009a). This general pattern was confirmed at various tidal flats (Alexander et al., 1991; Chang et al., 2006; Evans, 1965; Frey et al., 1989; Wang & Ke, 1997). The different dynamic processes of cohesive mud and non-cohesive sand can modify the classical cross-shore mud transport

mechanism. The interaction of sand-mud transport, cross-shore equilibrium bed profile, and sediment zonation is a key issue of the tidal flat morphodynamics. Especially, the existence of alongshore tidal currents will complicate the interaction, and the related cross-shore sediment transport mechanisms require further investigation.

The objective of this study is to investigate the sand-mud transport processes and the related morphological responses influenced by alongshore tidal currents, using field observations, numerical modeling, and primary analytical interpretations. The central Jiangsu coast, China, which is characterized by strong alongshore tidal currents and sand-mud tidal flat zonation, is a frequently investigated area of tidal flat sediment dynamics (Gao et al., 2009a, b; Ren et al., 1985; Wang & Ke, 1997; Yu et al., 2017; Zhang, 1992), and is chosen as the study area. On this basis, idealized numerical models were utilized to capture the first order characteristics obtained from observations. Further, the numerical models and analytical solutions help to understand the sand-mud flat dynamics.

2 Study Area

The study area is located at the central Jiangsu coast, China, which is situated between the Changjiang River estuary and abandoned Yellow River mouth (Figure 2a). Tides in this area are semi-diurnal and meso- to macro-tidal, with a mean tidal range of ca. 4 m (Wang Y.P. et al., 2012). Because of the southward propagation of the tidal wave, the offshore area is dominated by alongshore southward flood currents and northward ebb currents. Due to the landward flood and seaward ebb processes, the cross-shore components are also significant (Yu et al., 2017). The cross- and alongshore tidal waves are nearly standing, with the alongshore tidal wave relatively more progressive than the cross-shore tidal wave. The study area is sheltered by a large and shallow, radial-shaped tidal ridge (or linear sandbank) system (Figure 2a) (Liu et al., 1989; Ren, 1986; Wang Y. et al., 2012), so wave actions are weak. The offshore buoy 20 km north to the study area (Figure 2a) at the depth of 14 m shows that the annual mean significant wave height is 0.48 m. According to Hayes (1979), this area is tide-dominated.

Nowadays, with fine sediments being supplied from the erosion of the abandoned Yellow River Delta 100 km north to the study area, the coastline here has continued prograding seaward (Gao, 2009b; Wang Y.P. et al., 2012). The nearshore suspended sediment concentration (SSC) is

sufficiently high, and the tidally averaged SSC exceeds 1 kg/m^3 (Ren, 1986; Wang X.H. et al., 2011; Yu et al., 2014, 2017). The Dafeng harbor was constructed for freight traffic, in the north of the study area (Figure 2a). The construction of the sea wall started in early 2007 and finished in April 2008 (Figure 2b). Due to land reclamation, the intertidal area was all bare and subjected to a considerable reduction in cross-shore width (Wang Y.P. et al., 2012).

3 Methods

Firstly, field observations were undertaken across the intertidal flat, including measurements of sediment dynamics, sampling of water and surface sediment, and repetitive leveling. Secondly, on these basis schematized models were set up to further study the coevolution of hydrodynamics, sediment grain size, and morphology.

3.1 Field observation

Three sets of instruments were deployed across the intertidal flat (along the profile P1) to measure high-resolution sediment dynamics during May 5 – 12, 2008, just about one year after the beginning of the seawall construction (Figure 2b). Among them, a YSI/SonTek ADV ocean with D&A OBS–5+ was deployed on the upper intertidal flat (at station A08) 0.18 m above sea bed (asb). An observation system was placed at station M08 on the middle intertidal flat, which has six pairs of electromagnetic current meters and Seapoint turbidity sensors installed 0.38 – 1.12 m asb at Station M08. Further a TRDI WHS 1200 kHz ADCP was installed on a floating body at station S1 and S3, both near the mean low water level (MLWL). When water depth is smaller than 1.0 – 1.5 m, the proportion of blanking is too large, therefore effective depth-averaged velocities cannot be obtained using ADCP. During the measurements, water samples were collected at various depths to calibrate the OBS–5+ and Seapoint turbidities. High accuracy measurement of seabed level was undertaken along the profile P1 from the seawall front to the lower intertidal flat on May 13, 2008, and December 25, 2008, using a Magellan Z-MAX GPS. Details of the measurements, including SSC calibration statistics, can be found in Wang Y. P. et al. (2012).

3.2 Numerical Modeling

3.2.1 Model Description

The two-dimensional, depth-averaged (2DH) version of Delft3D was utilized, including the Delft3D-FLOW module, the Delft3D bed module for sand-mud mixtures, and the standard Exner equation for bathymetric evolution via sediment mass conservation (Deltares, 2014; Lesser, 2004; van Kessel et al., 2012). Two fractions of sediment were considered in the model, one being cohesive and the other being non-cohesive. Sediment transport of the cohesive and non-cohesive fractions was computed independently, which was analogous to other modeling works (Caldwell & Edmonds, 2014; Edmonds & Slingerland, 2010; Geleynse et al., 2011; Rossi et al., 2016; Tejedor et al., 2016). Erosion and deposition of cohesive sediment were calculated using the Partheniades-Krone formulations (Partheniades, 1965). The depth-averaged model for suspended sediment transport based on the asymptotic solution of the convection-diffusion equation was applied to calculate the erosion and deposition fluxes induced by non-cohesive sediment transport (Galappatti & Vreugdenhil, 1985; Wang, 1992). Due to the different dynamics of mixed-size sediments, bed composition is adjusted with the sorting processes beginning in the active layer. The changes are then progressively transferred to the underlying layers. Every new bed surface grain-size composition influences the subsequent sorting process, which eventually results in the change of the total sediment transport rate and bed-level. In this sense, a multi-layer strata concept was applied in the presence of multi-size sediment fractions. The “online” approach suggested by Roelvink (2006) was adopted, which speeds up bed adjustments by multiplying the bed level change in each time step by a morphological scale factor (MF).

3.2.2 Model Settings

The numerical model is schematized with a rectangular grid and a simple bathymetry based on the topography of the study area. The model domain is 35 km cross-shore and 20 km alongshore, consisting of 200 × 40 grid cells. In the cross-shore direction, within 15 km from the land boundary, the cell size is 125 m × 500 m, and the initial bed level decreases from 1 m to -9.5 m linearly, resulting in a 0.7 ‰ bed slope. The initial bed level starts from 1 m, which is consistent with the seawall foot’s elevation (land boundary) when it was constructed. In the rest of 20 km, the grid size is enlarged to 250 m × 500 m with uniform initial depth of 9.5m (Figure

3). In accordance with the observation, a cross-shore profile (CS) was defined with observation points O1, O2, and O3 to represent the anchored stations at the upper, middle, and lower intertidal flat, respectively. The focused area for monitoring the evolution of tidal flat morphology was also marked in Figure 3.

Boundary conditions of water level and sediment concentration are set according to the field circumstance. The tidal flat is sheltered by the subaerial sand ridges in the east. Because of the presence of a tidal channel parallel to the coastline, the flow in this region is mainly alongshore, and water level boundaries are applied only at the north and south edge of the model domain. According to the observed data (Wang Y.P. et al., 2012) and the validated regional tide model (Xing et al., 2012), the harmonic constituent M_2 is selected with an amplitude of 2 m, and the phase lag is defined to 12 degrees from the north to the south boundary. Observations show the existence of the coastal turbidity maximum at the study area. Suspended sediment (mainly mud) concentration reaches more than 1 kg/m^3 at the tidal flat, and decreases quickly to less than 0.5 kg/m^3 at 20 km offshore (Ren, 1986; Wang X.H. et al., 2011; Xing et al., 2010; Yu et al., 2014; 2017). Thus, on both boundaries, mud concentration decreases linearly from 1.25 kg/m^3 at the landward edge to 0.25 kg/m^3 at the seaward end, and sand concentration was derived from equilibrium profiles, which represent the local balance of current shear stress, water depth, and bed sediment grain size.

Both the drying and flooding threshold (Dryflc) and the threshold depth for computing sediment transport (SedThr) are 0.1 m. A uniform Manning coefficient of 0.016 s/m$^{1/3}$ is applied throughout the whole domain. The grain size of the sand fraction is 64 μm, and the dry bed density is 1600 kg/m^3. The mud parameters are also uniformly defined with settling velocity of 0.6 mm/s, critical shear stress for erosion and sedimentation of 0.15 Pa, erosion parameter of 2×10^{-4} kg/m^2/s, and dry bed density of 1000 kg/m^3. These parameters were selected to represent the local conditions to a great extent.

The initial bed stratigraphy is composed of 5 Lagrangian layers and 45 Eulerian layers, each 0.2 m thick, and the transport layer is defined to be 0.1 m thick. Bed composition is initially fully sand. Mud is only supplied from the open boundaries. The morphological scale factor MF was set to 20 to speed up bed adjustments. The simulation period in the model lasts 111 days, i.e., covers 6 years.

On the basis of the 1st year bathymetry and sediment conditions in the morphodynamic model, a short-term hydrodynamic simulation was carried out. The hydrodynamic and sediment transport processes can thus be investigated, together with the observed data.

4 Results

4.1 Observational Results

Observed cross-shore bed level and sediment grain-size profiles are shown in Figure 4a and 4c, respectively. The bed level along P1 showed convex-up cross-shore profiles, with an average slope of ~1.0 ‰. The bed elevation experienced significant accretion from May to December 2008 (Figure 4a). The accretion thickness ranged from 0.18 m to 0.63 m, with an average of 0.23 m along the profile.The seabed sediment coarsens seaward, with increasing sand content up to around 90 % near MLWL. Accompanied by sediment accretion, sand content of surface sediment mostly decreased along the profile during this period, to an extent of 20 – 40 %, especially at the middle intertidal flat (Figure 4c).

Hydrodynamic observation results are illustrated in Figure 5. Water depth reached up to about 0.8 m, 2.0 m and 4.0 m at the upper (A08), middle (M08) and lower (S1/S3) intertidal flat, respectively. The differences in cross-shore current velocities along the intertidal flat profile were not significant, and the cross-shore velocity components (V_c) ranged from -0.35 to 0.23 m/s. However, the alongshore tidal current speeds (V_l) were so different that it was maximally 0.98 m/s at the lower intertidal flat, at most 0.52 m/s at the middle intertidal flat, while nearly zero at the upper intertidal flat. At the lower intertidal flat (S1/S3), V_c varied almost symmetrically during a tidal cycle. V_l was obviously larger during flood periods, although the flood and ebb durations (based on the direction of V_l) were more or less the same, implying residual currents in the flood direction.

The maximum SSC can be more than 1.5 kg/m^3 at different parts of the intertidal flat (Figure 5). Due to uncertainties of calibration from ADCP backscatter intensity for high SSC, SSC at the lower intertidal flat (S1/S3) was not plotted. In most cases, SSC is larger at the middle flat than at the upper flat.

4.2 Model results

The modeled tidal flat morphology can be characterized by cross-shore profile adjustment and progradation. The alongshore differences in bed elevation of the intertidal flat are small throughout the modeling period (Figure 6). However, the cross-shore profile experienced significant accretion from the upper intertidal flat and kept prograding seaward. This character can be seen more clearly in the evolution of cross-section CS (Figures 6 and 7a). In the vertical direction, the whole intertidal flat profile accreted, where the upper part was mostly muddy with accumulation rates up to ca. 0.7 m/yr, and the lower part was mainly sandy with accumulation rates of more than one order smaller. Sequentially, convex-up tidal flat profiles formed and prograded seaward. The seaward progradation rate for the elevation of 1 m was ca. 875 m/yr in the first year, and gradually decreased to ca. 500 m/yr in the second and third year, 375 m/yr in the fourth and fifth year, and 250 m/yr in the sixth year. The continual progradation patterns based on symmetric tidal boundaries and waveless scenarios are consistent with other modeling works (Hu et al., 2015; Le Hir et al., 2007; Maan et al., 2015; Pritchard et al., 2002; Roberts et al., 2000).

The profile at the 4^{th} year is regarded as equilibrium in the model. Friedrichs (2011) defined an equilibrium tidal flat profile loosely as one with a shape that remains more or less constant over some characteristic period of natural forcing. In the third year the flat began to accrete up to the mean high water level (MHWL), and afterward, the top elevation kept prograding seaward. In the 4^{th} year, the shape of the tidal flat profile approached a steady state, when the convex-up profile was fully developed, and thereafter, the maximum bed slope on the flat is at the MWL.

Accompanied by the seaward progradation of the tidal flat, the cross-shore profile of sand content of surface sediment also moved progressively, indicating that surface sediment grain size is controlled by the flat elevation (Figure 7b). The upper flat is dominantly mud, while the lower flat is mostly sand. A mud layer of up to 2.2 m thick was thus preserved in the strata at the middle intertidal flat due to such progressive patterns of bed level and surface sediment grain size evolution (Figures 6 and 7a).

Figure 8 shows the modeled hydrodynamics during a tidal cycle at the observation points O1, O2, and O3, which represent the upper, middle and lower intertidal flat, respectively. The

maximal water depth at O1, O2, and O3 was 0.8 m, 2.0 m, and 4.0 m, corresponding to an inundation duration of 2.5, 5.5, and 10 hours. At the upper intertidal flat, the cross-shore current speed reached up to 0.24 m/s during flood and 0.23 m/s during ebb, while the alongshore tidal current velocities were nearly zero. Current velocities at the middle intertidal flat were comparable in both directions, but the cross-shore components were slightly larger: the maximum flood speed was 0.30 m/s cross-shore and 0.24 m/s alongshore, and the maximum ebb speed was 0.21 m/s cross-shore and 0.18 m/s alongshore. However, at the lower inter-tidal flat the alongshore tidal current velocities turned to be stronger, especially during the flood period. The maximum flood velocity component reached up to 0.48 m/s alongshore and 0.39 m/s cross-shore. The maximum ebb velocity component alongshore was 0.34 m/s, and 0.38 m/s cross-shore. Thus, the flood residual currents alongshore were also revealed at the lower flat.

The suspended particles were mainly mud, and the concentration of mud was mostly many orders of magnitude larger than that of sand. The largest mud concentration at O1, O2, and O3 was 1.3, 1.5, and 1.7 kg/m^3, respectively. At the upper and middle intertidal flat, the maximum SSC occurred when the cross-shore current velocities were the largest during the flood period (i.e. once inundated), while at the lower intertidal flat, the maximum SSC appeared when the water level is highest or lowest. It is worth noting that resuspension of sand only occurred at O3 during flood with maximum SSC of 1.4 kg/m^3, which caused the suspended sand transported landward and accumulated at the lower intertidal flat. In addition, according to the observed data, it is assumed that when water depth is smaller than 1.5 m, blanking is too large to get effective depth-averaged velocities in ADCP measurements. So, the light-yellow zones denote the estimated ADCP blanking at S1/S3 (Figures 2b and 5).

4.3 Comparisons between model results and observations

Although the schematized models cannot be compared directly with the observations, the models captured some key patterns and characteristics analogous to the measurements, concerning spatial variations of bed elevation and composition, hydrodynamics and sediment transport processes at the three observation points which represent different parts of the intertidal flat.

The modeled bed profiles were close to the observed in configurations. Bed level measurement along profile P1 (Figure 2b) was firstly undertaken in May 2008 (one year after the construction of the sea wall), and then in December 2008. To be compared with the observed data, the modeled bed elevation profile of the cross-section CS at the 1st and the 1.6th year was chosen. The selected width of the intertidal flat was also the same as the observations, i.e., approximately 3500 m from the land boundary to near MLWL. The modeled bed profile was also convex-up and kept accreting during the 0.6 years. The accretion thickness ranged from 0.05 m to 0.48 m, with an average of 0.25 m along the profile. These variations were all comparable with the observations. However, the average bed slope in the model is 0.8 ‰ in the first year and 0.9 ‰ in the 1.6th year, which is slightly smaller than the observed profile, indicating the modeled profile is less convex-up at the meantime (Figures 4a and 4b).

The modeled grain size of seabed sediment also coarsens in the seaward direction, with increasing sand content to 77 % maximally. These patterns were all consistent with the observed profiles, and in the observation of May 2008, the maximum sand content is around 73 %. Sand content of surface sediment in the model generally decreased along the profile during this period, as much as 30 % over the middle intertidal flat. In the observations, sand content decreased most at the middle intertidal flat to an extent of about 30 % as well (Figures 4c and 4d).

Meanwhile, the spatial and temporal variation patterns of modeled current velocities were also similar to the observations.The three observation points (O1, O2, and O3) were selected such that maximal water depth and inundation period were all similar to the measurements at the anchored stations. V_c changes a little at different parts of the intertidal flat, but V_l varies a lot at the three locations both in the model and observations. However, V_c is slightly larger and V_l is obviously smaller in the model (Figures 5 and 8).

The slightly larger V_c is attributed to the smaller modeled bed slope. It is derived from the continuity equation that V_c is controlled by the bed slope (Friedrichs & Aubrey, 1996). The modeled bed slope cross-shore is slightly smaller than observations (Figures 4a and 4b), resulting in larger V_c. Besides, ADCP blanking is too large to get effective depth-averaged velocities at small water depths. The estimated ADCP blanking at the lower intertidal flat (Figure 8) is likely to cover the maximum V_c. In other words, the model can obtain the peak values of V_c which are probably not measured by ADCP due to large blanking when water depth is small.

The smaller V_c can be interpreted by the differences in tidal range and bed friction. Assuming the alongshore water surface slope is uniform, the pressure difference in the alongshore direction is balanced by the bed friction in the first order simplification:

$$\rho g h s_l = \rho C_D (V_c^2 + V_l^2)^{1/2} V_l \quad (1)$$

in which ρ is water density, g is the gravitational acceleration, h is water depth, and s_l is the alongshore water surface slope. The relation of drag coefficient (C_D) and manning coefficient (n) is expressed as:

$$C_D = g n^2 / h^{1/3} \quad (2)$$

Combining equations (1) and (2) yields:

$$V_l = S_l h^{4/3} n^{-2} (V_c^2 + V_l^2)^{-1/2} \quad (3)$$

On the uppermost flat, where $V_c >> V_l$ (e.g., see Figure 5, 8), equation (3) reduces to:

$$V_l = S_l h^{4/3} n^{-2} V_c \quad (4)$$

while on the lowermost flat, if $V_l >> V_c$ (e.g., see Figure 5, 8), equation(3) reduces to:

$$V_l = s_l^{1/2} h^{2/3} n^{-1} \quad (5)$$

Therefore V_l increases with both local water depth and the alongshore water slope, while inversely proportional to the manning coefficient. The alongshore water surface slope in the model is smaller than observations due to a smaller tidal range or alongshore phase lag gradient. Furthermore, High SSC causes significant stratification of the water column, and thus induces drag reduction, so the drag coefficient or manning coefficient tends to be smaller than that in the model. These are all probably why the modeled V_l is smaller than observed.

Both observations and models suggest that tidally induced residual currents flow in the flood direction in shallow areas, which is consistent with previous studies (Charlton et al., 1975; Friedrichs et al., 1992; Kim et al., 2017; Li & O'Donnell, 1997, 2005; Robinson, 1960; Zimmerman, 1974). A nearly standing but slightly progressive tidal wave causes water depth to be greater during flood than ebb (Friedrichs et al., 1992). The h dependence in equation (3) then causes V_l to be stronger on flood in shallow areas where the relative difference in h between flood and ebb is most important. This is seen both in the above references and in the present observations and model results. Ebb is enhanced in deep channels in closed-ended tidal

345 embayments because continuity constraints require equal cross-sectionally integrated along-
346 system transport on ebb and flood. However, there is no such continuity constraint in the open
347 coast geometry here, so enhanced ebb flow in deeper water is not as relevant. Rather, the
348 strength of the flood-directed alongshore residual increases as one moves down from the upper
349 flat into deeper water because the power dependence of V_l on h is initially greater than 1. This
350 means the effect of deeper water on flood driving the residual is increasingly important with
351 increased water depth. In still deeper water, where $V_l >> V_c$ and the power dependence of V_l on h
352 decreases below 1, greater depth causes the strength of the alongshore residual flow to decrease
353 once more.

354 The model showed respectable consistencies compared to the measured SSCs. In most
355 cases, SSC decreased landward from the lower flat to the upper flat. The maximum SSC can be
356 around or even more than 1.5 kg/m^3 along the intertidal flat. In addition, the maximum SSC was
357 also associated with the dominant current velocity component. These all agree well with the
358 observed data (Figures 5 and 8). The slight deviations from the observations, which is mainly
359 reflected in the temporal variation patterns, is probably because waves were not involved in the
360 model, they inducing large SSCs in shallow water. It is noted that the observed SSC at the
361 middle flat (M08) station in Figure 5 often shows two peaks during each tidal cycle,
362 corresponding to resuspension by maximum velocity both on flood and on ebb. However, the
363 ebb SSC peak didn't arise in the model (O2 station in Figure 8), which is consistent with the
364 observed tidal cycles during 0:00 to 6:00 and 12:00 to 18:00, May 10, 2008 (Figure 5). This is
365 probably because these modeled and the observed tidal cycles are associated with a somewhat
366 larger asymmetry in alongshore flood versus ebb velocity, producing a greater asymmetry in
367 suspended resuspension during flood versus ebb.

368

369 **5 Discussion**

370 5.1 Impact of alongshore tidal currents

371 To investigate the influence of alongshore tidal currents, two more cases were set up in
372 addition to the reference case, in which the phase lag from the north to the south boundary is 12°.
373 All the other settings keeping the same, but the phase lag changed to 8° and 16°, respectively.

374 The alongshore water level gradient s_l can be derived as:

375 $$s_l = \frac{d}{dy}[a\cos(\omega t - \varphi)] = a\frac{\partial \varphi}{\partial y}\sin(\omega t - \varphi) \quad (6)$$

376 where a and ω are tidal level amplitude and angular frequency of M_2 tidal current constituent,
377 respectively, and φ is the phase in radian. V_l is proportional to the square root of the alongshore
378 water surface slope (equation (5)), and the amplitude of the alongshore water surface slope is
379 proportional to the tidal amplitude and alongshore phase gradient (equation (6)). Therefore, V_l
380 can be enhanced by increasing the phase lag alongshore.

381 Besides, short-term hydrodynamic simulations were also carried out. Based on the 4th
382 year bathymetry and hydrodynamic conditions of each case (with a phase lag of 8°, 12°, and 16°),
383 when morphology is regarded as approaching equilibrium, hydrodynamic simulations were set
384 up with the same phase lag in the morphodynamic model. So the hydrodynamics, sediment and
385 morphological characteristics at quasi-equilibrium were investigated among the cases with
386 different alongshore phase lags.

387 The 4th year bed elevation of the intertidal flat in the other two cases show the same
388 characters as the reference case in the alongshore direction (Figure 6). Thus, sensitivity analysis
389 only focused differences of the cross-shore profile CS (Figures 9a and 9b). The upper flat is mud
390 dominated and had almost the same cross-shore profiles in all cases. At the middle and lower flat,
391 the differences between the cases were significant. Here we use sand content of ~25 % as the
392 transition between sand dominated and mud dominated (see the dashed lines in grey in Figure 9).
393 If the sand content of surface sediment is larger than 25 %, the flat is categorized to mixed and
394 sand dominated (hereinafter called 'sand flat' in short); while the flat with sand content lower
395 than 25% is regarded as 'mud flat'.

396 Sand flat expands landward when the phase lag increases. In case 1 (red curve) with a
397 phase lag of 8°, the whole intertidal flat was mainly composed of mud, and the bed profile is
398 almost a uniform slope of ~0.8 ‰. However, in case 2 (black curve, with phase lag of 12°), the
399 lower flat is sandy and the mean bed slope is ~0.7 ‰, and in case 3 (blue curve, with phase lag
400 of 16°), the sand flat even expands from the lower flat to the middle flat with a smaller mean
401 slope of ~0.5 ‰. The bed slope of the transition zone between the mud and sand flat is much
402 steeper: ~1.6 ‰ in case 2 and ~1.7 ‰ in case 3 (Figures 9a and 9b).

Short-term hydrodynamics based on the 4th year morphology (equilibrium tidal flat profiles) in the three cases were also compared. According to equations (5) and (6), the alongshore tidal currents are positively related to water depth and alongshore phase lag, and the former has a larger impact. Therefore, on the mud flat where the bed profiles and water depths are very close, V_l is mainly controlled by alongshore phase lag, and is largest in the 16° case, smallest in the 8° case. However, bed shear stress and morphodynamics on the upper mud flat in all three cases are controlled more by V_c, because V_c is much larger than V_l there. On the sand flat where the bed profiles vary a lot, V_l is mainly controlled by water depth. Accordingly, the 12° case has the largest V_l then (Figure 9c). V_c is controlled by the cross-shore bed slope, and thus have little difference on the mud flat. But on the sand flat, the 16° case has the largest V_c induced by the mildest bed slope (Figure 9d). On the sand flat, V_l and V_c are both important to bottom shear stress and morphodynamics because of similar magnitudes, and in some areas, V_l is even larger than V_c.

The dynamic equilibrium theory of tidal flat is used to interpret the model results. It assumes that morphological equilibrium is associated with spatially uniform tidally maximum bed shear stress (τ_{max}) (Friedrichs, 2011). If the flat profile is static, τ_{max} is equal to the critical bed shear stress (Friedrichs & Aubrey, 1996). This theory has been supported by many observational and modeling studies (Bearman et al., 2010; Chen et al., 2010; Hu et al., 2015; Hsu et al., 2013; Kirby, 2000; Pritchard & Hogg, 2003; Pritchard et al., 2002; van der Wegen & Jaffe, 2014).

In this study, the modeled upper flat has steady shapes and the flat profiles kept prograding seaward. Such uniform distributions of τ_{max} also exist on the mud flat and the values are almost the same in the three cases with different alongshore phase lags. This agrees with the above researches. However, the mean value of the uniformly distributed τ_{max} on the mud flat is ca. 0.3 Pa, which is twice of the critical shear stress of mud (0.15 pa) in the model (Figure 9e). This is probably because the high SSC results in large deposition rates, and the uniform τ_{max} has to be enhanced so as to balance the deposition (Friedrichs, 2011; Hu et al., 2015).

Meanwhile, on the sand flat in the 12° and 16° cases, τ_{max} are greatly enhanced up to ~1.0 Pa and spatially varying. The dashed arrows indicate the turning points of τ_{max} in these two cases, which are both corresponding to the transitions between mud and sand flat (Figure 9a, e).

Possible interpretations are proposed. Firstly, only a single sediment fraction was taken into account in the dynamic equilibrium theory, while two factions (a mud fraction and a sand fraction) were involved in our models. The spatial variations of sediment grain size lead to different dynamic properties, relating to different τ_{max}. Secondly, at the 4^{th} year in the models, the shape of mud flat profiles was steady but the sand flat profiles were still changing. Therefore the uniform τ_{max} on the sand flats does not exist.

Furthermore, responses of hydrodynamics, sediment transport and morphology to the variation of V_l were also studied. Starting from the 1st year bathymetry and sediment conditions of the reference case (see the cross-shore profiles of intertidal flat in Figure 4b, d), short-term hydrodynamic simulations were undertaken with the alongshore phase lag of 8°, 12° and 16°, respectively. Equations (5) and (6) show that the alongshore tidal current is enhanced with increasing phase lag (Figure 10a). Due to the identical cross-shore bed slope, the cross-shore tidally maximum flood current speeds exhibit little difference with changing alongshore phase lag (Figure 10b). In response to such hydrodynamic conditions, the tidally averaged SSC of mud and sand were also increased by the enhancement of alongshore tidal currents (Figures 10c and 10d). Sand concentration is 0 at the upper and middle flat and quickly increases from lower flat to sub-flat area. The maximum tidally-averaged SSC of sand in the 16° case is up to 0.002 kg/m^3, which is 8 times that of the 12° case, and 1400 times of the 8° case.

During flood, the strong alongshore tidal currents (the 16° case) at the lower flat cause resuspension of mud, and the cross-shore tidal currents bring it onshore where it then settled due to weakening current speed. Mud thus accreted on the upper intertidal flat, while mud eroded and left relict sand at the lower part, shaping a steeper cross-shore bed profile (Figure 10e). Likewise, sand can also be resuspended by increased alongshore tidal currents mainly from the subtidal-flat (Figure 10d) and accumulated on the lower intertidal flat (Figure 10f). The area where sands accumulated corresponds to where mud was eroded (Figures 10e and 10f). These morphological and sedimentological responses explain the cross-shore profiles of bed elevation and sand content at the quasi-equilibrium states (Figures 9a and 9b).

In the 8° case with relatively weak alongshore tidal currents, mud accumulated across the whole intertidal flat, and at the lower flat, the deposition rate increased seaward (Figure 10e), resulting in a milder cross-shore bed slope and an increase of mud content at lower flat. There

was no suspended sand across the whole flat and the sand deposition rates were all zero, so the intertidal flat tend to be fully muddy (Figure 10f). These trends were also confirmed in Figures 9a and 9b.

5.2 Mechanisms of landward sand transport

A two-dimensional (both cross-shore and alongshore tidal currents included) analytical solution was obtained to express the tidal residual sand transport. The mechanisms of the landward sand transport can thus be further analyzed.

In the nearshore shallow area of the present model (Figure 3), due to the homogeneous bathymetry alongshore, the cross-shore (X direction) residual tidal current is zero. But the alongshore (Y direction) residual tidal current exists. Current velocities in X and Y directions can be expressed as follows. Assuming that the amplitude of M_2 tidal constituent dominates the current velocity, $\varepsilon_{\mathrm{Ui}}$ and $\varepsilon_{\mathrm{V}i}$ are in the order of 10^{-1}.

Velocity in X direction:

$$\begin{aligned} U(t) &= U_2\cos(\omega t - \phi_{\mathrm{U2}}) + U_4\cos(2\omega t - \phi_{\mathrm{U4}}) \\ &= U_2[\cos(\omega t - \phi_{\mathrm{U2}}) + \varepsilon_{\mathrm{U4}}\cos(2\omega t - \phi_{\mathrm{U4}})] \end{aligned} \quad (7)$$

Velocity in Y direction:

$$\begin{aligned} V(t) &= V_0 + V_2\cos(\omega t - \phi_{\mathrm{V2}}) + V_4\cos(2\omega t - \phi_{\mathrm{V4}}) \\ &= V_2[\varepsilon_{\mathrm{V0}} + \cos(\omega t - \phi_{\mathrm{V2}}) + \varepsilon_{\mathrm{V4}}\cos(2\omega t - \phi_{\mathrm{V4}})] \end{aligned} \quad (8)$$

in which:

V_0 = residual current in Y direction;

ω = angular frequency of M_2 tidal current constituent;

U_{i} = amplitude of the other tidal current constituent in X direction, e.g. U_2 is related to M_2 constituent, and U_4 corresponds to M_4;

V_{i} = amplitude of the other tidal current constituent in Y direction;

ϕ_{Ui} = phase of tidal constituent M_i in X direction;

ϕ_{Vi} = phase of tidal constituent M_i in Y direction;

$$\varepsilon_{\mathrm{Ui}} = \frac{U_i}{U_2} \quad (i = 4);$$

$$\varepsilon_{\mathrm{V}i} = \frac{V_i}{V_2} \quad (i = 0\ or\ 4)$$Because the settling velocities of sand are relatively large, 3.3 mm/s for 64 um sand, the phase lag of sand concentration to velocity is relatively small (Yu et al., 2011, 2012), suggesting the approximately local balance of suspended sand and tidal current shear stress. According to Friedrichs and Aubrey (1988), Gräwe et al. (2014) and Olaberrieta et al. (2018), instantaneous sand transport rate is proportional to cubic of current velocity. Thus, the residual transport rate of non-cohesive sediment (sand) during an M_2 period in the X direction is:

$$\overline{q_x} = \frac{1}{T}\int_0^T q_x(t)dt$$

$$q_x(t) = k(U(t)^2 + V(t)^2)U(t) \tag{9}$$

where T is the M_2 tidal period, k is a constant.

By omitting the small quantities of third order ($O(\epsilon^3)$), it is derived:

$$\frac{\overline{q_x}}{kU_2^3} = A + B + C$$

$$A = \varepsilon_{\mathrm{v0}}\,\alpha^2\cos(\phi_{\mathrm{U2}} - \phi_{\mathrm{V2}})$$

$$\mathrm{B} = \frac{1}{4}\varepsilon_{\mathrm{U4}}[3\cos(2\phi_{\mathrm{U2}} - \phi_{\mathrm{U4}}) + \alpha^2\cos(2\phi_{\mathrm{v2}} - \phi_{\mathrm{U4}})]$$

$$C = \frac{1}{2}\varepsilon_{V4}\alpha^2\cos(\phi_{U2} + \phi_{V2} - \phi_{V4})$$

$$\alpha = V_2/U_2 \tag{10}$$

In the present study area where slightly progressive M_2 tidal waves prograde southward (in the alongshore direction), the phases of M_2 constituent in X and Y directions are close nearshore, which is supported by the observed and modeled hydrodynamics (Figure 5, 8), and also the harmonic analysis results of tidal velocities measured at a sub-tidal station near the study area (cf. Supporting information). Thus it is assumed that $\phi_{\mathrm{U2}} = \phi_{\mathrm{V2}} = \phi_2$, and the above equations can be further simplified as:

$$A = \frac{3}{2}\varepsilon_{\mathrm{v0}}\alpha^2$$

$$B = \frac{1}{4}\varepsilon_{\mathrm{U4}}(3 + \alpha^2)\cos(2\phi_2 - \phi_{\mathrm{U4}})$$

$$C = \frac{1}{2}\varepsilon_{V4}\alpha^2 \cos(2\phi_2 - \phi_{V4}) \quad (11)$$

Therefore, the residual sand transport in X (cross-shore) direction ($\overline{q_x}$) is scaled by 3th power of U_2. *A*, *B*, and *C* are non-dimensional terms, and their analytical expressions reveal the mechanisms of the cross-shore residual sand transport.

Term *A* is residual current related, the direction of which is controlled by Y residual current, and magnitude is proportional to the magnitude of the Y residual current and the ratio of the M_2 tidal current amplitude in Y direction to X direction (α). It is then suggested that negative Y (southward (flood) direction in the present model) residual currents generate negative X (westward (flood) direction in the present model) residual sand transport, and the strong Y M_2 tidal amplitude enlarges α, so as to enhance the magnitude of *A*. Both observations and modeling indicated that when the alongshore phase lag is large (e.g. the 16° case), the alongshore residual currents are southward ((flood) "–") and the α value is quite large at the lower and sub-tidal flat, the landward sand transport is thus induced. In case of the Jiangsu Coast, the observations at a sub-tidal station near the study area (cf. Supporting information) also show the strong alongshore residual currents in the flood direction and a large α value.

Term *B* and *C* are related to tidal asymmetry in X (cross-shore) and Y (alongshore) direction, respectively. The M_4 currents are not only in X direction but also Y direction and contribute to the cross-shore residual sand transport. The phase lag of $(2\phi_2 - \phi_{U4})$ and $(2\phi_2 - \phi_{V4})$ determine their directions, and the relative amplitude of M_4 currents (ε_{U4} and ε_{V4}) and α control the magnitudes. In the shallow areas, the larger ratio of tidal amplitude to water depth promotes flood-dominant tidal asymmetries (Friedrichs et al., 1992) . Because both the positive X and Y are ebb directions, flood-dominant tidal asymmetries correspond to the 90° to 270° phase lag of $(2\phi_2 - \phi_{U4})$ and $(2\phi_2 - \phi_{V4})$. Thus, terms *B* and *C* are negative, indicating westward/landward residual sand transport.

It is worth noting that the relative importance of the Y (alongshore) tidal currents (represented by α) is crucial to the sum of *A*, *B*, and *C*. If α is sufficiently smaller than 1, term *A* and *C* will reduce to a small value and term $B = \frac{3}{4}\varepsilon_{U4}\cos(2\phi_2 - \phi_{U4})$, suggesting that the X (cross-shore) residual sand transport is then only caused by the cross-shore tidal asymmetry. However, if α is sufficiently larger than 1, like the observations at the lower flat station (Figure 5)

the above part of X (cross-shore) tidal asymmetry (i.e. $\frac{3}{4}\varepsilon_{\mathrm{U4}}\cos(2\phi_2 - \phi_{\mathrm{U4}})$) will only account for a small fraction of term *B*, and all three terms (*A*, *B*, and *C*) will be controlled by α^2.

According to equations (5) and (6), under the same bathymetry in the present model, the alongshore tidal currents increase proportionally to the square root of the alongshore phase lag (Figure 10a). But the consequent X (cross-shore) residual sand transport will increase much more quickly (equation (11)). This partly explains the mechanisms of the landward sand transport and the sandy lower flat formation, which are induced by the strong alongshore tidal currents.

In contrast, if slightly progressive M_2 tidal waves prograde northward, the M_2 phase in X direction deviates ~180° from Y direction ($\phi_{\mathrm{U2}} + \pi = \phi_{\mathrm{V2}}$).

$$A = -\frac{3}{2}\varepsilon_{\mathrm{v0}}\alpha^2$$

$$B = \frac{1}{4}\varepsilon_{\mathrm{U4}}(3 + \alpha^2)\cos(2\phi_{\mathrm{U2}} - \phi_{\mathrm{U4}})$$

$$C = -\frac{1}{2}\varepsilon_{V4}\alpha^2\cos(2\phi_{\mathrm{V2}} - \phi_{V4}) \quad (12)$$

Similarly, the northward (positive) residual current velocity results in the negative (westward/landward) *A*. Terms *B* and *C* are also controlled by the tidal asymmetry. The positive X and Y are associated with the ebb and the flood direction, respectively. Flood-dominant tidal asymmetries correspond to the 90° to 270° phase lag of $(2\phi_{\mathrm{U2}} - \phi_{\mathrm{U4}})$ and the -90° to 90° phase lag of $(2\phi_{\mathrm{V2}} - \phi_{\mathrm{V4}})$, suggesting westward/landward residual sand transport as well due to negative terms of *B* and *C*. Numerical models also show that tidal flat morphology and sediment zonation are not influenced by a reversed direction of tidal wave propagation.

The above cases are associated with an only slightly progressive M_2 constituent in the alongshore direction. However, due to a large scale and low frictions in the alongshore direction and a small scale in the cross-shore direction, it is worth considering a case where the alongshore tidal wave is purely progressive and the cross-shore tidal wave is purely standing. In this case, $\phi_{\mathrm{U2}} = \phi_{\mathrm{V2}} - \frac{\pi}{2}$, and then equation (10) can be simplified as:

$$A = 0$$

$$B = \frac{1}{4}\varepsilon_{\mathrm{U4}}(3 - \alpha^2)\cos(2\phi_{\mathrm{U2}} - \phi_{\mathrm{U4}})$$

$$C = \frac{1}{2}\varepsilon_{V4}\alpha^2 \sin(2\phi_{\mathrm{V2}} - \phi_{V4}) \quad (13)$$

The above solution suggests that if the alongshore and cross-shore tidal velocities are 90 degrees out of phase, the alongshore residual currents are irrelevant to the cross-shore residual sand transport (A = 0). Without the presence of the alongshore tidal velocities (α = 0), term B is controlled by the peak velocity asymmetry in the cross-shore direction ($\cos(2\phi_{\mathrm{U2}} - \phi_{\mathrm{U4}})$). However, the amplified alongshore M_2 tidal velocity amplitude can reduce the term B, and the large α can even change the direction of term B. The direction of term C is controlled by $\sin(2\phi_{\mathrm{V2}} - \phi_{V4})$, which represents the slack water duration asymmetry rather than the peak velocity assymentry in the alongshore direction. The most flood-dominated alongshore tidal currents with $2\phi_{\mathrm{V2}} - \phi_{V4}$ of 0°, which means term C equals to zero, can not result in cross-shore residual sand transport. This is pronouncedly different from the above cases.

5.3 Future works

This study is based on the case of Jiangsu coast, China, and the role of alongshore tidal currents on sand/mud transport and tidal flat morphodynamics was investigated. However, for a comprehensive understanding, more field examples and sensitivity analysis are required with different settings, such as tidal range, alongshore tidal properties (standing to progressive), initial bed profile, boundary sand and mud concentrations, etc. The analytical solution helps to understand the cross-shore transport of sand, however, similar two-dimensional solutions of the cross-shore transport of mud are more complicated due to the temporal and spatial settling lags and their effects on horizontal advection. It could be developed based on one-dimensional solutions (Yu et al., 2012).

Observational (Andersen et al., 2006; Christiansen, 2006; Deloffre et al., 2005, 2007; Fan et al., 2006; Marion et al., 2009; Shi et al., 2017; Wang et al., 2009; Yang et al., 2003, 2008) and modeling (Fagherazzi, et al, 2007; Hu et al., 2015; Maan et al., 2015; Roberts et al., 2000) works both revealed that waves have important impacts on the morphology and sediment grain size of tidal flats. So future research should couple the effects of cross-shore and alongshore tidal currents, as well as waves.

584 Here we only considered one mud fraction and one sand fraction in the models. In fact,
585 both sand and mud can be divided into more fractions of different properties. Models using more
586 sediment fractions would provide more details regarding the processes of sediment transport and
587 morphological evolution, especially at the transitions between the mud flat and sand flat (Chou et
588 al., 2018; Guillou et al., 2009; van der Wegen & Jaffe, 2014; Wang et al., 2014, 2016).

589 Sediment transport of sand and mud was calculated separately. However, interactions
590 exist between sand and mud. If it is taken into account in the erosion formulae, a distinction is
591 made when the mud content remains below a critical value, the regime is non-cohesive, and
592 otherwise, it switches to cohesive (van Ledden et al., 2004; van Rijn, 2007). Models with sand-
593 mud interactions were suggested, and the performance of this method needs further evaluation
594 (Braat et al., 2017; Carniello et al., 2012; Dufois et al., 2014; Le Hir et al., 2011; Paarlberg et al.,
595 2005; Ulses et al., 2008; van Ledden et al., 2006).

596 During the observation periods, the whole intertidal flat was bare. Thus the role of
597 biological processes and salt marshes were not considered in the models. But marshes may
598 colonize the upper flat and expand over time. It is then necessary to observe and simulate the
599 biomorphodynamic processes of intertidal flats, which were discussed by a number of studies
600 (D'Alpaos et al., 2007; Fagherazzi et al., 2012; Kirwan & Murray, 2007; Marani et al., 2010;
601 Mariotti & Fagherazzi, 2010; Mudd et al., 2010; Schwarz et al., 2014; Tambroni & Seminara,
602 2012).

603

604 **6 Conclusions**

605 In addition to cross-shore tidal currents, the alongshore components also play an
606 important role in sediment transport, morphological evolution, and sediment grain-size change in
607 the cross-shore direction of the tidal flat. With an increase in the background alongshore tidal
608 water level phase lag, the alongshore currents are gradually dominant on the lower flat. In
609 contrast, the upper flat is always dominated by cross-shore currents, which are controlled by the
610 cross-shore bed profile. Thus, in case of different alongshore tidal currents, bed profiles at the
611 upper flats are quite similar, being convex-up and consist of mud. However, strong alongshore
612 currents can erode the mud at the lower flat, and promote the landward sand transport from the
613 subtidal area to the lower flat, forming a sand flat. The tidally maximum bed shear stress is

almost spatially uniform across the muddy area of the cross-shore profile, but bed stresses are pronouncedly elevated when the bed sediment coarsens at the lower flat.

Acknowledgments

We thank Jia Jianjun, Gao Jianhua, Yang Yang, Du Xiaoqin, Xing Fei, Li Jiasheng, Liu Yunling, Cheng Jun, Wang Huaqiang, and Ran Qi for participating in the field work. We thank Li Runxiang for modifying Figure 2. This study is supported by the National Natural Science Foundation of China (41676077, 41676081), and the Fundamental Research Funds for the Central Universities (2016B00814). Y.P. Wang acknowledges the funding from the National Natural Science Foundation of China (41625021). Data in support of this manuscript are available at https://figshare.com/projects/2018JC014550/60053#. We highly acknowledge Carl Friedrichs and an anonymous reviewer for their constructive and valuable suggestions that allowed for an improvement of the quality of the manuscript.

References

Alexander C. R., Nittrouer, C. A., DeMaster, D. J., Park, Y.-A., & Park, S.-C. (1991). Macrotidal mudflats of west Korea: a model for interpretation of intertidal deposits. *Journal of Sedimentary Research*, *61*(5), 805–824. https://doi.org/10.1306/D42677DA-2B26-11D7-8648000102C1865D

Amos, C. L. (1995). Siliclastic tidal flats. In G. M. E. Perillo (Ed), *Geomorphology and sedimentology of estuaries* (pp. 273–306). Amsterdam: Elsevier.

Andersen, T. J., Pejrup, M., & Nielsen, A. A. (2006). Long-term and high-resolution measurements of bed level changes in a temperate, microtidal coastal lagoon. *Marine Geology*, *226*, 115–125. doi:10.1016/j.margeo.2005.09.016

Anderson, F.E. (1973). Observations of some sedimentary processes acting on a tidal flat. *Marine Geology*, *14*(2), 101–116. https://doi.org/10.1016/0025-3227(73)90054-6

Bartholdy, J., & Kvale, E. P. (2006). Introduction to proceedings from 6th international conference on tidal sedimentology. *Marine Geology*, *235*, 1–4. doi: 10.1016/j.margeo.2006.10.024

Bearman, J. A., Friedrichs, C. T., Jaffe, B. E., & Foxgrover, A. C. (2010). Spatial trends in tidal flat shape and associated environmental parameters in South San Francisco Bay. *Journal of Coastal Research*, *26*(2), 342–349. https://doi.org/10.2112/08-1094.1

643 Braat, L., van Kessel, T., Leuven, J. R. F. W., & Kleinhans, M. G. (2017). Effects of mud supply on
644 large-scale estuary morphology and development over centuries to millennia. *Earth Surface*
645 *Dynamics, 5*, 617–652. doi:10.5194/esurf-5-617-2017

646 Caldwell, R. L., & Edmonds, D. A. (2014). The effects of sediment properties on deltaic processes and
647 morphologies: A numerical modeling study. *Journal of Geophysical Research: Earth Surface*, *119*,
648 961–982. doi:10.1002/2013JF002965

649 Carniello, L., Defina, A., & D'Alpaos, L. (2012). Modeling sand-mud transport induced by tidal currents
650 and wind waves in shallow microtidal basins: Application to the Venice Lagoon (Italy). *Estuarine,*
651 *Coastal and Shelf Science*, *102–103*, 105–115. http://dx.doi.org/10.1016/j.ecss.2012.03.016

652 Chang, T.S., Bartholomä, A., & Flemming, B.W. (2006). Seasonal dynamics of fine-grained sediments in
653 a back-barrier tidal basin of the German Wadden Sea (southern North Sea). *Journal of Coastal*
654 *Research, 22*(2), 328–338. doi:10.2112/03-0085.1

655 Charlton, J. A., McNicoll, W., & West, J. R. (1975). Tidal and freshwater induced circulation in the Tay
656 Estuary. *Proceedings of the Royal Society of Edinburgh, Section B: Biological Sciences*, *75*(1–2),
657 11–27. doi:10.1017/S0308211300002504

658 Chen, S.-N., Geyer, W. R., Sherwood, C. R., & Ralston, D. K. (2010). Sediment transport and deposition
659 on a river dominated tidal flat: An idealized model study. *Journal of Geophysical Research*, *115*,
660 C10040. doi:10.1029/2010JC006248

661 Chou, Y. - J., Nelson, K. S., Holleman, R. C., Fringer, O. B., Stacey, M. T., Lacy, J. R., et al. (2018).
662 Three - dimensional modeling of fine sediment transport by waves and currents in a shallow estuary.
663 *Journal of Geophysical Research: Oceans*, *123*, 4177–4199. https://doi.org/10.1029/2017JC013064

664 Christiansen, C., Vølund, G., Lund-Hansen, L.C., & Bartholdy, J. (2006). Wind influence on tidal flat
665 sediment dynamics: Field investigations in the Ho Bugt, Danish Wadden Sea. *Marine Geology*,
666 *235*(1–4), 75–86. https://doi.org/10.1016/j.margeo.2006.10.006

667 Collins, M. B., Amos, C. L., & Evans, G. (1981). Observations of some sediment - transport processes
668 over intertidal flats, the Wash, U.K.. In S. Nio, R.T. Shüttenhelm, T.C. Van Weering (Eds.),
669 *Holocene marine sedimentation in the North Sea basin*. doi:10.1002/9781444303759.ch6

670 D'Alpaos, A., Lanzoni, S., Marani, M., & Rinaldo, A. (2007). Landscape evolution in tidal embayments:
671 Modeling the interplay of erosion, sedimentation, and vegetation dynamics. *Journal of Geophysical*
672 *Research*, *112*, F01008. doi:10.1029/2006JF000537

673 Deloffre, J., Lafite, R., Lesueur, P., Lesourd, S., Verney, R., & Gue´zennec, L. (2005). Sedimentary
674 processes on an intertidal mudflat in the upper macrotidal Seine estuary, France. *Estuarine, Coastal*
675 *and Shelf Science, 64,* 710–720. https://doi.org/10.1016/j.ecss.2005.04.004

676 Deloffre, J., Verney, R., Lafite, R., Lesueur, P., Lesourd, S., & Cundy, A. (2007). Sedimentation on
677 intertidal mudflats in the lower part of macrotidal estuaries: Sedimentation rhythms and their
678 preservation. *Marine Geology, 241,* 19–32. doi:10.1016/j.margeo.2007.02.011

679 Deltares (2014). *Delft3D-FLOW, Simulation of multi-dimensional hydrodynamic flows and transport*
680 *phenomena, including sediments, User manual* (version: 3.15.34158). Retrieved from
681 https://oss.deltares.nl/documents/183920/185723/Delft3D-FLOW_User_Manual.pdf

682 Dufois, F., Verney, R., Le Hir, P., Dumas, F., & Charmasson, S. (2014). Impact of winter storms on
683 sediment erosion in the Rhone River prodelta and fate of sediment in the Gulf of Lions (North
684 Western Mediterranean Sea). *Continental Shelf Research, 72,* 57–72.
685 https://doi.org/10.1016/j.csr.2013.11.004

686 Dyer, K. R. (2000). Preface. *Continental Shelf Research, 20,* 1037–1038. https://doi.org/10.1016/S0278-
687 4343(00)00010-8

688 Edmonds, D. A., & Slingerland, R. L. (2010). Significant effect of sediment cohesion on delta
689 morphology. *Nature Geoscience, 3*(2), 105–109. doi:10.1038/NGEO730

690 Engelund, F., & Hansen E. (1967). *A monograph on sediment transport in alluvial streams*. Copenhagen:
691 Teknisk Forlag.

692 Evans, G. (1965). Intertidal flat sediments and their environments of deposition in the Wash. *Quarterly*
693 *Journal of the Geological Society, 121,* 209–240. http://dx.doi.org/10.1144/gsjgs.121.1.0209

694 Fagherazzi, S., Kirwan, M. L., Mudd, S. M., Guntenspergen, G. R., Temmerman, S., D'Alpaos, A., et al.
695 (2012). Numerical models of salt marsh evolution: Ecological, geomorphic, and climatic factors.
696 *Reviews of Geophysics, 50,* RG1002, doi:10.1029/2011RG000359

697 Fagherazzi, S., Palermo, C., Rulli, M. C., Carniello, L., & Defina, A. (2007). Wind waves in shallow
698 microtidal basins and the dynamic equilibrium of tidal flats. *Journal of Geophysical Research, 112,*
699 F0204. doi:10.1029/2006JF000572

700 Fan, D. (2012). Open-coast tidal flats. In R.A. Davis, Jr., R.W. Dalrymple (Eds.), *Principles of tidal*
701 *sedimentology* (pp. 187–229). Dordrecht: Springer.

Fan, D., Guo, Y., Wang, P., & Shi, J. Z. (2006). Cross-shore variations in morphodynamic processes of an open-coast mudflat in the Changjiang Delta, China: With an emphasis on storm impacts. *Continental Shelf Research*, *26*, 517–538. doi:10.1016/j.csr.2005.12.011

Flemming, B. W. (2003). Tidal flats. In G. V. Middlenton (Ed.), *Encyclopedia of sediments and sedimentary rocks* (pp. 734–737). Dordrecht: Kluwer.

Flemming, B. W., & Bartholomä, A. (Eds.) (1995). *Tidal signatures in modern and ancient sediments* (IAS Special Publication No. 24). Oxford: Blackwell Science. doi:10.1002/9781444304138

French, P. (1997). *Coastal and estuarine management*. London: Routledge. https://doi.org/10.4324/9780203437278

Frey, R. W., Howard, J. D., Han, S.-J., & Park, B.-K. (1989). Sediments and sedimentary sequences on a modern macrotidal flat, Inchon, Korea. *Journal of Sedimentary Research*, *59*(1), 28–44. https://doi.org/10.1306/212F8F0D-2B24-11D7-8648000102C1865D

Friedrichs, C. T. (2011). Tidal flat morphodynamics: A synthesis. In E. Wolanski, D. McLusky (Eds.), *Treatise on estuarine and coastal science* (pp. 137–170). Waltham: Academic Press.

Friedrichs, C. T., & Aubrey, D. G. (1988). Non-linear tidal distortion in shallow well mixed estuaries: A synthesis. *Estuarine, Coastal and Shelf Science*, *27*(5), 521–545. https://doi.org/10.1016/0272-7714(88)90082-0

Friedrichs, C. T., & Aubrey, D. G. (1996). Uniform bottom shear stress and equilibrium hyposometry of intertidal flats. In C. Pattiaratchi (Ed), *Coastal and estuarine studies* (Vol. 50, pp. 405–429). Washington, DC: American Geophysical Union.

Friedrichs, C. T., Lynch, D. R., & Aubrey, D. G. (1992). Velocity asymmetries in frictionally-dominated tidal embayments: Longitudinal and lateral variability. In D. Prandle (Ed), *Dynamics and exchanges in estuaries and the coastal zone* (Vol. 40, pp. 277–312). American Geophysical Union. https://doi.org/10.1029/CE040p0277

Galappatti, G., & Vreugdenhil, C. B. (1985). A depth-integrated model for suspended sediment transport. *Journal of Hydraulic Research*, *23*(4), 359–377. https://doi.org/10.1080/00221688509499345

Gao, S. (2009a). Geomorphology and sedimentology of tidal flats. In G. M. E. Perillo, E. Wolanski, D. Cahoon, M. Brinson (Eds.), *Coastal wetlands: An ecosystem integrated approach* (pp. 295–316). Amsterdam: Elsevier.

731 Gao, S. (2009b). Modeling the preservation potential of tidal flat sedimentary records, Jiangsu coast,
732 eastern China. *Continental Shelf Research*, *29*(16), 1927–1936.
733 https://doi.org/10.1016/j.csr.2008.12.010

734 Geleynse, N., Storms, J. E. A., Walstra, D.-J. R., Jagers, H. R. A., Wang, Z. B., & Stive, M. J. F. (2011).
735 Controls on river delta formation; insights from numerical modelling. *Earth and Planetary Science*
736 *Letters*, *302*(1), 217–226. doi:10.1016/j.epsL2010.12.013

737 Gräwe, U., Burchard, H., Müller, M., & Schuttelaars, H. M. (2014). Seasonal variability in M_2 and M_4
738 tidal constituents and its implications for the coastal residual sediment transport. *Geophysical*
739 *Research Letters, 41*(15), 5563–5570. https://doi.org/10.1002/2014GL060517

740 Guillou, N., Chapalain, G., & Thais, L. (2009). Three-dimensional modeling of tide-induced suspended
741 transport of seabed multicomponent sediments in the eastern English Channel. *Journal of*
742 *Geophysical Research*, *114*, C07025. doi:10.1029/2008JC004791

743 Hayes, M. O. (1979). Barrier island morphology as a function of tidal and wave regime. In S. P.
744 Leatherman (Ed.), *Barrier islands from the Gulf of St. Lawrence to the Gulf of Mexico* (pp. 211–
745 236). New York: Academic Press.

746 Hsu, T.-J., Chen, S.-N., & Ogston, A. S. (2013). The landward and seaward mechanisms of fine-sediment
747 transport across intertidal flats in the shallow-water region—A numerical investigation. *Continental*
748 *Shelf Research, 60*, S85–S98. https://doi.org/10.1016/j.csr.2012.02.003

749 Hu, Z., Wang, Z. B., Zitman, T. J., Stive, M. J. F., & Bouma, T. J. (2015). Predicting long-term and short-
750 term tidal flat morphodynamics using a dynamic equilibrium theory. *Journal of Geophysical*
751 *Research: Earth Surface*, *120*(9), 1803–1823. https://doi.org/10.1002/2015JF003486

752 Kim, B.-G., & Cho, Y.-K. (2017). Tide-induced residual circulation in a bay with laterally asymmetric
753 depth. *Journal of Geophysical Research: Oceans*, *122*(5), 4040–4050.
754 https://doi.org/10.1002/2016JC012473

755 Kirby, R. (2000). Practical implications of tidal flat shape. *Continental Shelf Research*, *20*(10), 1061-
756 1077. https://doi.org/10.1016/S0278-4343(00)00012-1

757 Kirwan, M. L., & Murray, A. B. (2007). A coupled geomorphic and ecological model of tidal marsh
758 evolution. *Proceedings of the National Academy of Sciences*, *104*(15), 6118–6122.
759 doi:10.1073/pnas.0700958104

Le Hir, P., Cayocca, F., & Waeles, B. (2011). Dynamics of sand and mud mixtures: A multiprocess-based modelling strategy. *Continental Shelf Research*, *31*(10, Supplement), S135–S149. https://doi.org/10.1016/j.csr.2010.12.009

Le Hir, P., Monbet, Y., & Orvain, F. (2007). Sediment erodability in sediment transport modelling: Can we account for biota effects? *Continental Shelf Research*, *27*(8), 1116–1142. https://doi.org/10.1016/j.csr.2005.11.016

Le Hir, P., Roberts, W., Cazaillet, O., Christie, M., Bassoullet, P., & Bacher, C. (2000). Characterization of intertidal flat hydrodynamics. *Continental Shelf Research*, *20*(12), 1433–1459. https://doi.org/10.1016/S0278-4343(00)00031-5

Lesser, G. R., Roelvink, J. A., van Kester, J. A. T. M., & Stelling, G. S. (2004). Development and validation of a three-dimensional morphological model. *Coastal Engineering*, *51*(8), 883–915. https://doi.org/10.1016/j.coastaleng.2004.07.014

Li, C., & O'Donnell, J. (2005). The effect of channel length on the residual circulation in tidally dominated channels. *Journal of Physical Oceanography*, *35*(10), 1826–1840. https://doi.org/10.1175/JPO2804.1

Li, C., & O'Donnell, J. (1997). Tidally driven residual circulation in shallow estuaries with lateral depth variation. *Journal of Geophysical Research: Oceans*, *102*(C13), 27915–27929. https://doi.org/10.1029/97JC02330

Liu, Z. Huang, Y., & Zhang, Q. (1989). Tidal current ridges in the southwestern Yellow Sea. *Journal of Sedimentary Research*, *59*(3), 432–437. https://doi.org/10.1306/212F8FB7-2B24-11D7-8648000102C1865D

Maan, D. C., van Prooijen, B. C., Wang, Z. B., & De Vriend, H. J. (2015). Do intertidal flats ever reach equilibrium? *Journal of Geophysical Research: Earth Surface*, *120*(11), 2406–2436. https://doi.org/10.1002/2014JF003311

Mangor, K., Drønen, N. K., Kærgaard, K. H., & Kristensen, S. E. (2017). *Shoreline management guidelines*. Hørsholm: DHI.

Marani, M., D'Alpaos, A., Lanzoni, S., Carniello, L., & Rinaldo, A. (2010). The importance of being coupled: Stable states and catastrophic shifts in tidal biomorphodynamics. *Journal of Geophysical Research: Earth Surface*, *115*(F4). https://doi.org/10.1029/2009JF001600

Marion, C., Anthony, E. J., & Trentesaux, A. (2009). Short-term (≤2 yrs) estuarine mudflat and saltmarsh sedimentation: High-resolution data from ultrasonic altimetery, rod surface-elevation table, and filter

traps. *Estuarine, Coastal and Shelf Science*, *83*(4), 475–484. https://doi.org/10.1016/j.ecss.2009.03.039

Mariotti, G., & Fagherazzi, S. (2010). A numerical model for the coupled long-term evolution of salt marshes and tidal flats. *Journal of Geophysical Research: Earth Surface*, *115*(F1). https://doi.org/10.1029/2009JF001326

Mudd, S. M., D'Alpaos, A., & Morris, J. T. (2010). How does vegetation affect sedimentation on tidal marshes? Investigating particle capture and hydrodynamic controls on biologically mediated sedimentation. *Journal of Geophysical Research: Earth Surface*, *115*(F3). https://doi.org/10.1029/2009JF001566

Nittrouer, C. A., Raubenheimer, B., & Wheatcroft, R. A. (2013). Lessons learned from comparisons of mesotidal sand- and mudflats. *Continental Shelf Research*, *60*, S1-S12. https://doi.org/10.1016/j.csr.2013.03.003

Olabarrieta, M., Geyer, W. R., Coco, G., Friedrichs, C. T., & Cao, Z. (2018). Effects of density - driven flows on the long - term morphodynamic evolution of funnel - shaped estuaries. *Journal of Geophysical Research: Earth Surface*, *123*, 2901–2924. https://doi.org/10.1029/2017JF004527

Paarlberg, A. J., Knaapen, M. A. F., de Vries, M. B., Hulscher, S. J. M. H., & Wang, Z. B. (2005). Biological influences on morphology and bed composition of an intertidal flat. *Estuarine, Coastal and Shelf Science*, *64*(4), 577–590. https://doi.org/10.1016/j.ecss.2005.04.008

Partheniades, E. (1965). Erosion and deposition of cohesive soils. *Journal of the Hydraulics Division*, *91*(1), 105–139.

Pritchard, D., & Hogg, A. J. (2003). Cross-shore sediment transport and the equilibrium morphology of mudflats under tidal currents. *Journal of Geophysical Research: Oceans*, *108*(C10). https://doi.org/10.1029/2002JC001570

Pritchard, D., Hogg, A. J., & Roberts, W. (2002). Morphological modelling of intertidal mudflats: the role of cross-shore tidal currents. *Continental Shelf Research*, *22*(11), 1887–1895. https://doi.org/10.1016/S0278-4343(02)00044-4

Quaresma, V. d. S., Bastos, A. C., & Amos, C. L. (2007). Sedimentary processes over an intertidal flat: A field investigation at Hythe flats, Southampton Water (UK). *Marine Geology*, *241*(1), 117–136. https://doi.org/10.1016/j.margeo.2007.03.009

Reise, K. (2001). *Ecological comparison of sedimentary shores*. Berlin: Springer-Verlag.

Ren, M. E. (Ed.) (1986). *Comprehensive investigation of the coastal zone and tidal land resources of Jiangsu Province* (in Chinese). Beijing: Ocean Press.

Ren, M. E., Zhang, R. S., & Yang, J. H. (1985). Effect of typhoon no. 8114 on coastal morphology and sedimentation of Jiangsu Province, People's Republic of China. *Journal of Coast Research, 1*(1), 21–28.

Roberts, W., Le Hir, P., & Whitehouse, R. J. S. (2000). Investigation using simple mathematical models of the effect of tidal currents and waves on the profile shape of intertidal mudflats. *Continental Shelf Research*, *20*(10), 1079–1097. https://doi.org/10.1016/S0278-4343(00)00013-3

Robinson, A. H. W. (1960). Ebb-flood channel systems in sandy bays and estuaries. *Geography*, *45*(3), 183–199.

Roelvink, J. A. (2006). Coastal morphodynamic evolution techniques. *Coastal Engineering*, *53*(2), 277–287. https://doi.org/10.1016/j.coastaleng.2005.10.015

Rossi, V. M., Kim, W., López, J. L., Edmonds, D., Geleynse, N., Olariu, C., et al. (2016). Impact of tidal currents on delta-channel deepening, stratigraphic architecture, and sediment bypass beyond the shoreline. *Geology*, *44*, 927–930. doi: 10.1130/G38334.1

Schwarz, C., Ye, Q. H., van der Wal, D., Zhang, L. Q., Bouma, T., Ysebaert, T., & Herman, P. M. J. (2014). Impacts of salt marsh plants on tidal channel initiation and inheritance. *Journal of Geophysical Research: Earth Surface*, *119*(2), 385–400. https://doi.org/10.1002/2013JF002900

Shi, B. W., Yang, S. L., Wang, Y. P., Li, G. C., Li, M. L., Li, P., & Li, C. (2017). Role of wind in erosion-accretion cycles on an estuarine mudflat. *Journal of Geophysical Research: Oceans*, *122*(1), 193–206. https://doi.org/10.1002/2016JC011902

Tambroni, N., & Seminara, G. (2012). A one-dimensional eco-geomorphic model of marsh response to sea level rise: Wind effects, dynamics of the marsh border and equilibrium. *Journal of Geophysical Research: Earth Surface*, *117*(F3). https://doi.org/10.1029/2012JF002363

Tejedor, A., Longjas, A., Caldwell, R., Edmonds, D. A., Zaliapin, I., & Foufoula-Georgiou, E. (2016). Quantifying the signature of sediment composition on the topologic and dynamic complexity of river delta channel networks and inferences toward delta classification. *Geophysical Research Letters, 43*, 3280–3287. doi:10.1002/2016GL068210

Temmerman, S., Meire, P., Bouma, T. J., Herman, P. M. J., Ysebaert, T., & De Vriend, H. J. (2013). Ecosystem-based coastal defence in the face of global change. *Nature, 504*, 79–83. https://doi.org/10.1038/nature12859

Ulses, C., Estournel, C., Durrieu de Madron, X., & Palanques, A. (2008). Suspended sediment transport in the Gulf of Lions (NW Mediterranean): Impact of extreme storms and floods. *Continental Shelf Research*, *28*(15), 2048–2070. https://doi.org/10.1016/j.csr.2008.01.015

van der Wegen, M., & Jaffe, B. E. (2014). Processes governing decadal-scale depositional narrowing of the major tidal channel in San Pablo Bay, California, USA. *Journal of Geophysical Research: Earth Surface*, *119*(5), 1136–1154. https://doi.org/10.1002/2013JF002824

van Kessel, T., Spruyt-de Boer, A., van der Werf, J., Sittoni, L., van Prooijen, B. C., Winterwerp, H. (2012). *Bed module for sand-mud mixtures, in framework of BwN project NTW 1.3 mud dynamics* (draft). Delft: Deltares.

van Ledden, M., van Kesteren, W. G. M., & Winterwerp, J. C. (2004). A conceptual framework for the erosion behaviour of sand–mud mixtures. *Continental Shelf Research*, *24*(1), 1–11. https://doi.org/10.1016/j.csr.2003.09.002

van Ledden, M., Wang, Z.-B., Winterwerp, H., & de Vriend, H. (2006). Modelling sand–mud morphodynamics in the Friesche Zeegat. *Ocean Dynamics*, *56*(3), 248–265. https://doi.org/10.1007/s10236-005-0055-9

van Rijn, L. C. (2007). Unified View of Sediment Transport by Currents and Waves. I: Initiation of Motion, Bed Roughness, and Bed-Load Transport. *Journal of Hydraulic Engineering*, *133*(6), 649–667. https://doi.org/10.1061/(ASCE)0733-9429(2007)133:6(649)

Wang, A., Gao, S., Chen, J., & Li, D. (2009). Sediment dynamic responses of coastal salt marsh to typhoon “KAEMI” in Quanzhou Bay, Fujian Province, China. *Chinese Science Bulletin*, *54*(1), 120–130. https://doi.org/10.1007/s11434-008-0365-7

Wang, X. H., Qiao, F., Lu, J., & Gong, F. (2011). The turbidity maxima of the northern Jiangsu shoal-water in the Yellow Sea, China. *Estuarine, Coastal and Shelf Science*, 93(3), 202–211. https://doi.org/10.1016/j.ecss.2010.10.020

Wang, X., & Ke, X. (1997). Grain-size characteristics of the extant tidal flat sediments along the Jiangsu coast, China. *Sedimentary Geology*, *112*(1), 105–122. https://doi.org/10.1016/S0037-0738(97)00026-2

Wang, Y. P., Gao, S., Jia, J., Thompson, C. E. L., Gao, J., & Yang, Y. (2012). Sediment transport over an accretional intertidal flat with influences of reclamation, Jiangsu coast, China. *Marine Geology*, *291–294*, 147–161. https://doi.org/10.1016/j.margeo.2011.01.004

Wang, Y., Gao, S., & Jia, J. (2006). High-resolution data collection for analysis of sediment dynamic processes associated with combined current-wave action over intertidal flats. *Chinese Science Bulletin*, *51*(7), 866–877. https://doi.org/10.1007/s11434-006-0866-1

Wang, Y., Yu, Q., Gao, S., & Flemming, B. (2014). Modeling the effect of progressive grain-size sorting on the scale dependence of back-barrier tidal basin morphology. *Continental Shelf Research*, *91*, 26–36. https://doi.org/10.1016/j.csr.2014.09.006

Wang, Y., Yu, Q., Jiao, J., Tonnon, P. K., Wang, Z. B., & Gao, S. (2016). Coupling bedform roughness and sediment grain-size sorting in modelling of tidal inlet incision. *Marine Geology*, *381*, 128–141. https://doi.org/10.1016/j.margeo.2016.09.004

Wang, Y., Zhang, Y., Zou, X., Zhu, D., & Piper, D. (2012). The sand ridge field of the South Yellow Sea: Origin by river–sea interaction. *Marine Geology*, *291–294*, 132–146. https://doi.org/10.1016/j.margeo.2011.01.001

Wang, Z. B. (1992). Theoretical analysis on depth-integrated modelling of suspended sediment transport. *Journal of Hydraulic Research*, *30*(3), 403–421. https://doi.org/10.1080/00221689209498927

Xing, F., Wang, Y. P., & Wang, H. V. (2012). Tidal hydrodynamics and fine-grained sediment transport on the radial sand ridge system in the southern Yellow Sea. *Marine Geology*, *291–294*, 192–210. https://doi.org/10.1016/j.margeo.2011.06.006

Xing, F., Wang, Y., Gao, J., & Zou, X. (2010). Seasonal distributions of the concentrations of suspended sediment along Jiangsu coastal sea (in Chinese with English abstract). *Oceanologia et Limnologia Sinica*, *41*(3), 1–10.

Yang, S. L., Li, H., Ysebaert, T., Bouma, T. J., Zhang, W. X., Wang, Y. Y., et al. (2008). Spatial and temporal variations in sediment grain size in tidal wetlands, Yangtze Delta: On the role of physical and biotic controls. *Estuarine, Coastal and Shelf Science*, *77*(4), 657–671. https://doi.org/10.1016/j.ecss.2007.10.024

Yang, S.-L., Friedrichs, C. T., Shi, Z., Ding, P.-X., Zhu, J., & Zhao, Q.-Y. (2003). Morphological response of tidal marshes, flats and channels of the Outer Yangtze River mouth to a major storm. *Estuaries*, *26*(6), 1416–1425. https://doi.org/10.1007/BF02803650

Yu, Q., Flemming, B. W., & Gao, S. (2011). Tide-induced vertical suspended sediment concentration profiles: phase lag and amplitude attenuation. *Ocean Dynamics*, *61*(4), 403–410. https://doi.org/10.1007/s10236-010-0335-x

912 Yu, Q., Wang, Y. P., Flemming, B., & Gao, S. (2012). Tide-induced suspended sediment transport:
913 Depth-averaged concentrations and horizontal residual fluxes. *Continental Shelf Research*, *34*, 53–
914 63. https://doi.org/10.1016/j.csr.2011.11.015

915 Yu, Q., Wang, Y. W., & Gao, S. (2014). Tide and continental shelf circulation induced suspended
916 sediment transport on the Jiangsu Coast: winter observations out of Xinyanggang (in Chinese, with
917 English abstract). *Journal of Nanjing University (natural sciences)*, *50*, 625–634.

918 Yu, Q., Wang, Y., Shi, B., Wang, Y. P., & Gao, S. (2017). Physical and sedimentary processes on the
919 tidal flat of central Jiangsu Coast, China: Headland induced tidal eddies and benthic fluid mud
920 layers. *Continental Shelf Research*, *133*, 26–36. https://doi.org/10.1016/j.csr.2016.12.015

921 Zhang, R. (1992). Suspended sediment transport processes on tidal mud flat in Jiangsu Province, China.
922 *Estuarine, Coastal and Shelf Science*, *35*(3), 225–233. https://doi.org/10.1016/S0272-
923 7714(05)80045-9

924 Zimmerman, J. T. F. (1974). Circulation and water exchange near a tidal watershed in the dutch wadden
925 sea. *Netherlands Journal of Sea Research*, *8*(2), 126–138. https://doi.org/10.1016/0077-
926 7579(74)90013-1

927

928 **Figure captions**

929 **Figure 1**. Sketch of sand-mud tidal flat influenced by cross-shore and alongshore tidal currents
930 (MHWL, MWL, and MLWL denotes mean high water level, mean water level and mean low
931 water level, respectively, modified from Friedrichs (2011)).

932 **Figure 2**. (a) Maps of the study area and the location of the intertidal flats at Dafeng, Jiangsu,
933 China; (b) Sites of field measurements in 2008: A08, M08, and S1/S3 are anchor stations for
934 hydrodynamic measurements, and P1 is the bed level profile (modified from Wang Y.P. et al.
935 (2012)).

936 **Figure 3**. Grid and initial bathymetry (O1, O2, and O3: observation points, CS: cross-section,
937 red rectangle: focused area. Bed elevation: 0 m refers to the mean sea level).

938 **Figure 4**. Observed and modeled bed elevation and sand content of surface sediment along the
939 profile P1 in Figure 2b (The observed elevation is with reference to the national datum1985, in
940 which 0 m is the long-term mean sea level of the Yellow Sea).

941 **Figure 5**. Observational hydrodynamics: time series of water depth, depth-averaged velocity,
942 and SSC measured at the upper (A08, blue line), middle (M08, green line), and lower (S1/S3, red
943 line) intertidal flat. Locations of the stations are marked in Figure 2b. V_c and V_l are the current
944 velocity components across (offshore (ebb) "+" and onshore (flood) "−") and along (northward
945 (ebb) "+" and southward (flood) "−") the intertidal flat, respectively.

946 **Figure 6**. (a, b, c, d) Modeled bathymetry in the focused area in Figure 3; (e, f, g, h) Bed
947 elevation and stratigraphy of the cross-section CS.

948 **Figure 7**. Temporal variations of (a) bed elevation and (b) sand content of surface sediment
949 along the cross-shore profile CS.

950 **Figure 8**. Modeled hydrodynamics: time series of water depth, depth-averaged velocity, and SSC
951 at O1 (blue line), O2 (green line), and O3 (red line) during a tidal cycle form the 1st year in the
952 flat's evolution of the reference case. V_c and V_l are the current velocity components across
953 (offshore (ebb) "+" and onshore (flood) "−") and along (northward (ebb) "+" and southward
954 (flood) "−") the intertidal flat, respectively. Areas in light yellow are estimated ADCP blanking
955 at S1/S3 (Figure 2b and 5), corresponding to water depth smaller than 1.5 m.

956 **Figure 9**. Comparison of (a) bed elevation, (b) sand content of surface sediment; tidally
957 maximum flood current speed (c) alongshore and (d) cross-shore; and (e) tidally maximum bed
958 shear stress magnitude along the cross-shore profile CS at the 4th year in the three cases. The
959 dashed arrows indicate the turning points of τ_{max} in the 12° and 16° cases, which are also
960 corresponding to the transitions between mud and sand flat.

961 **Figure 10.** Modeled hydrodynamics (based on the 1st year bathymetry and hydrodynamic
962 conditions of the reference case) along the cross-shore profile CS: tidally maximum flood current
963 speed (a) alongshore and (b) cross-shore; tidally averaged SSC of (c) mud and (d) sand; and
964 variations of available mass of (e) mud and (f) sand in a tidal cycle.

Figure 1.

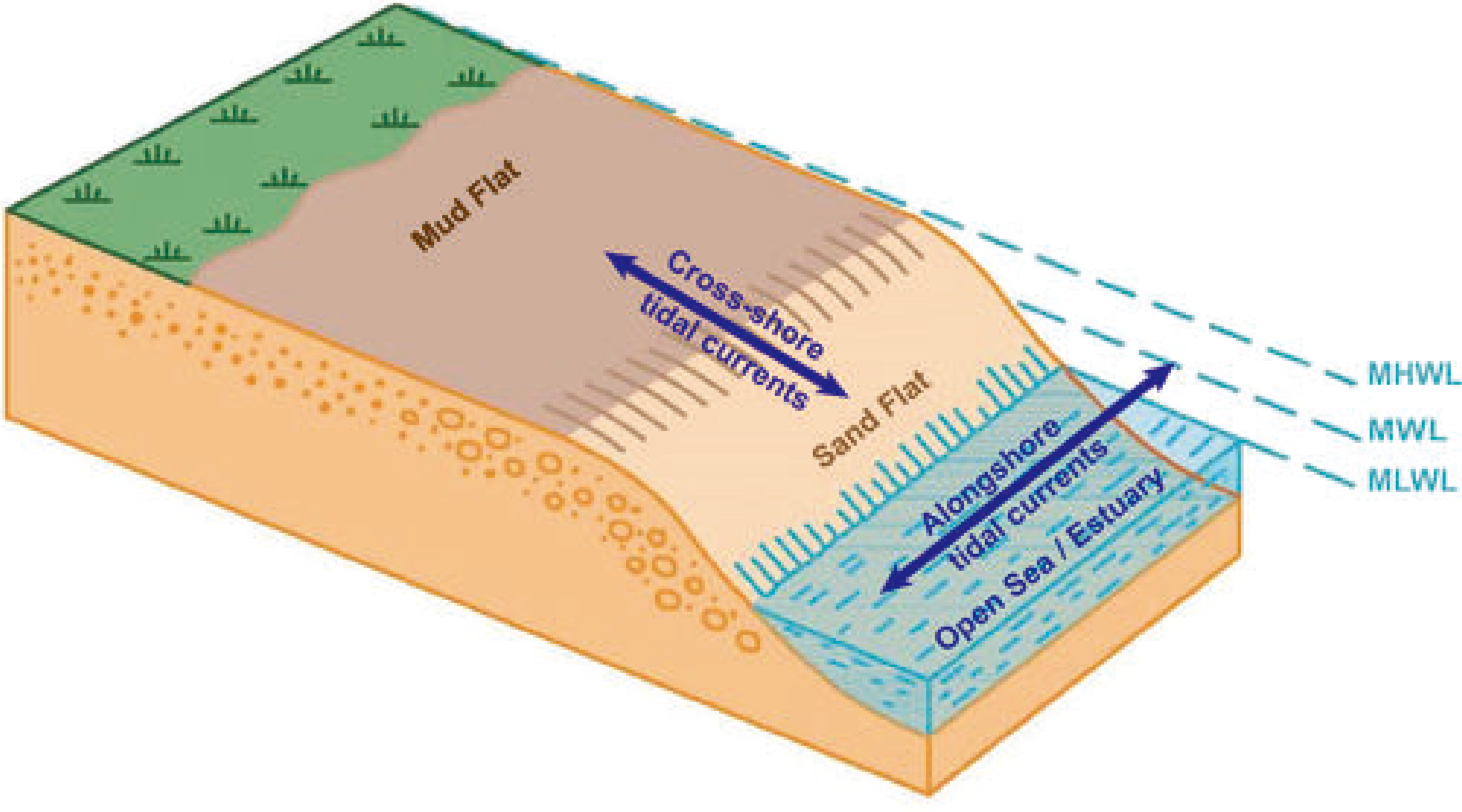
Mud Flat
Cross-shore
tidal currents
Sand Flat
Alongshore
tidal currents
Open Sea / Estuary
MHWL
MWL
MLWL

Figure 2.

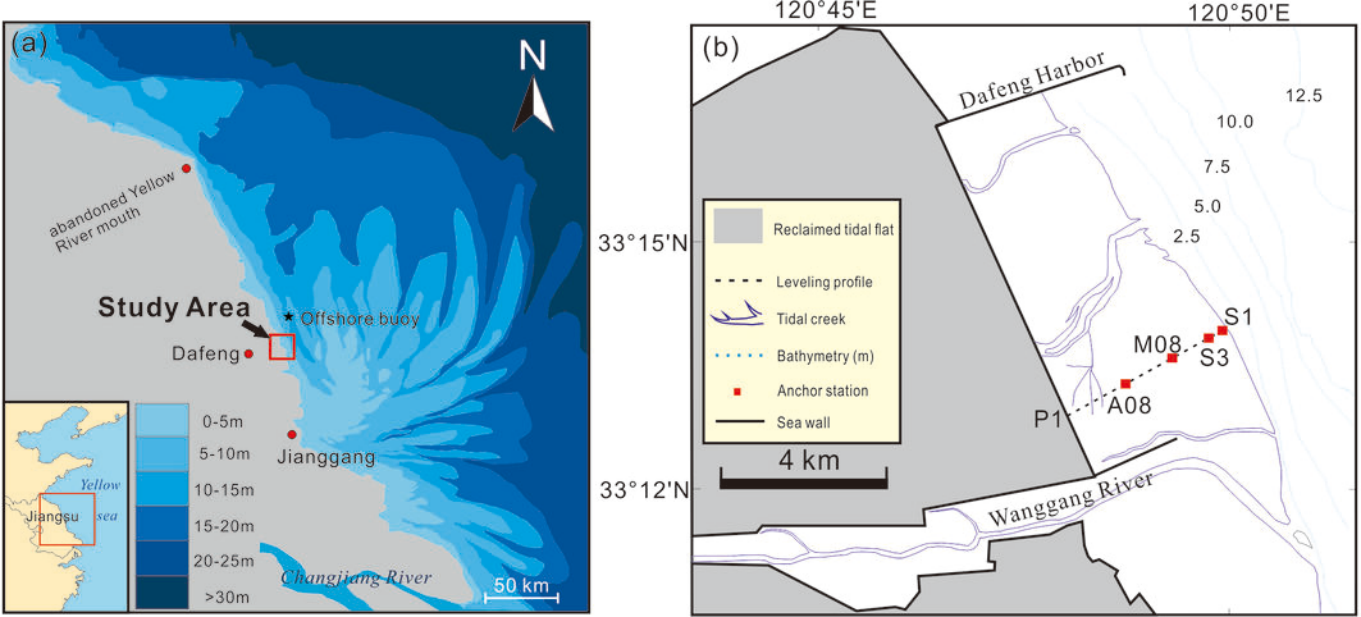
(a)
N
abandoned Yellow River mouth
Study Area
Offshore buoy
Dafeng
Jianggang
Yellow sea
Jiangsu
0-5m
5-10m
10-15m
15-20m
20-25m
>30m
Changjiang River
50 km
(b)
120°45'E
120°50'E
33°15'N
33°12'N
Dafeng Harbor
12.5
10.0
7.5
5.0
2.5
Reclaimed tidal flat
Leveling profile
Tidal creek
Bathymetry (m)
Anchor station
Sea wall
4 km
S1
M08
S3
A08
P1
Wanggang River

Figure 3.

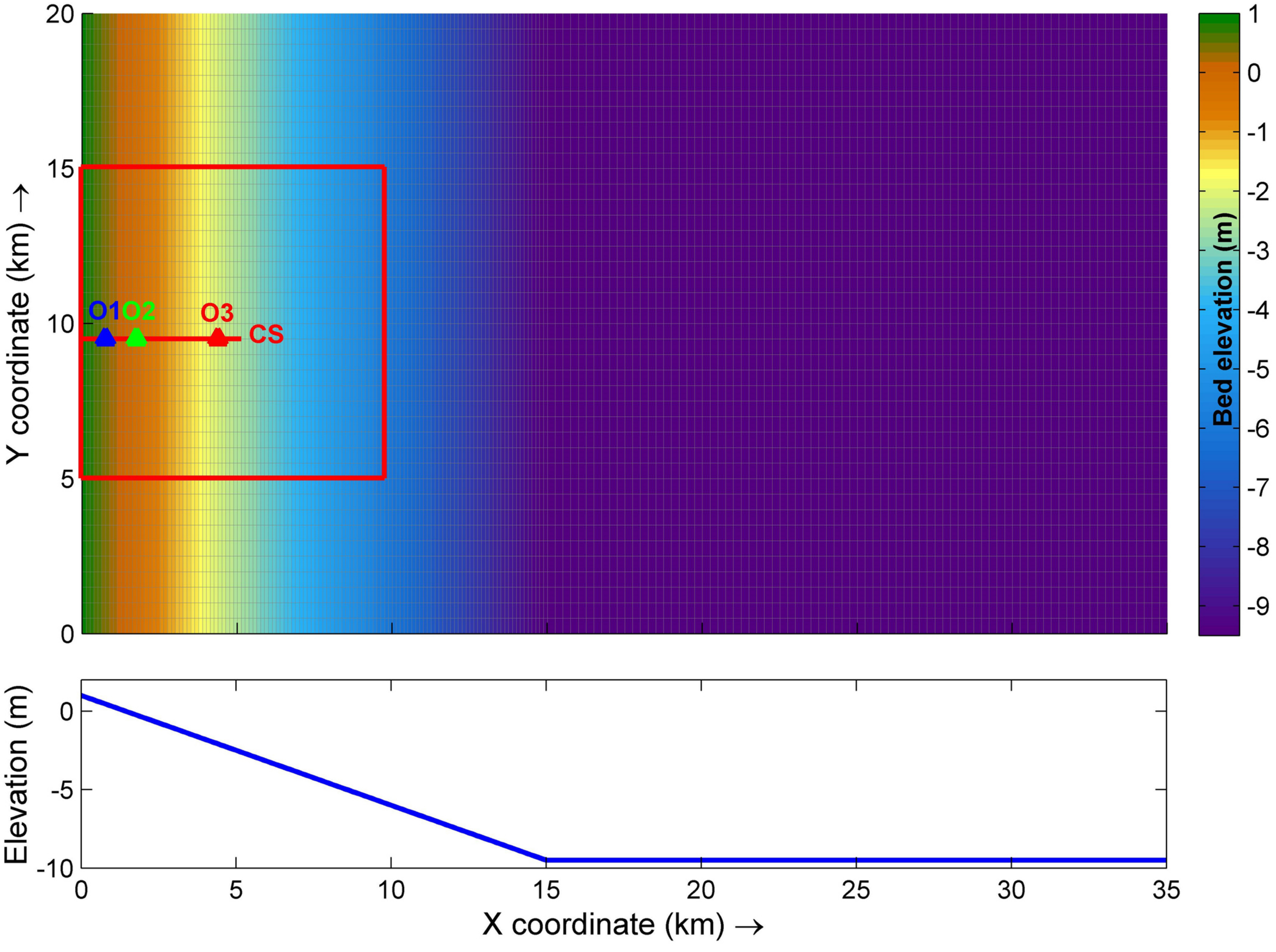
Y coordinate (km) →
20
15
10
5
0
O1
O2
O3
CS
Bed elevation (m)
1
0
-1
-2
-3
-4
-5
-6
-7
-8
-9
Elevation (m)
0
-5
-10
0
5
10
15
20
25
30
35
X coordinate (km) →

Figure 4.

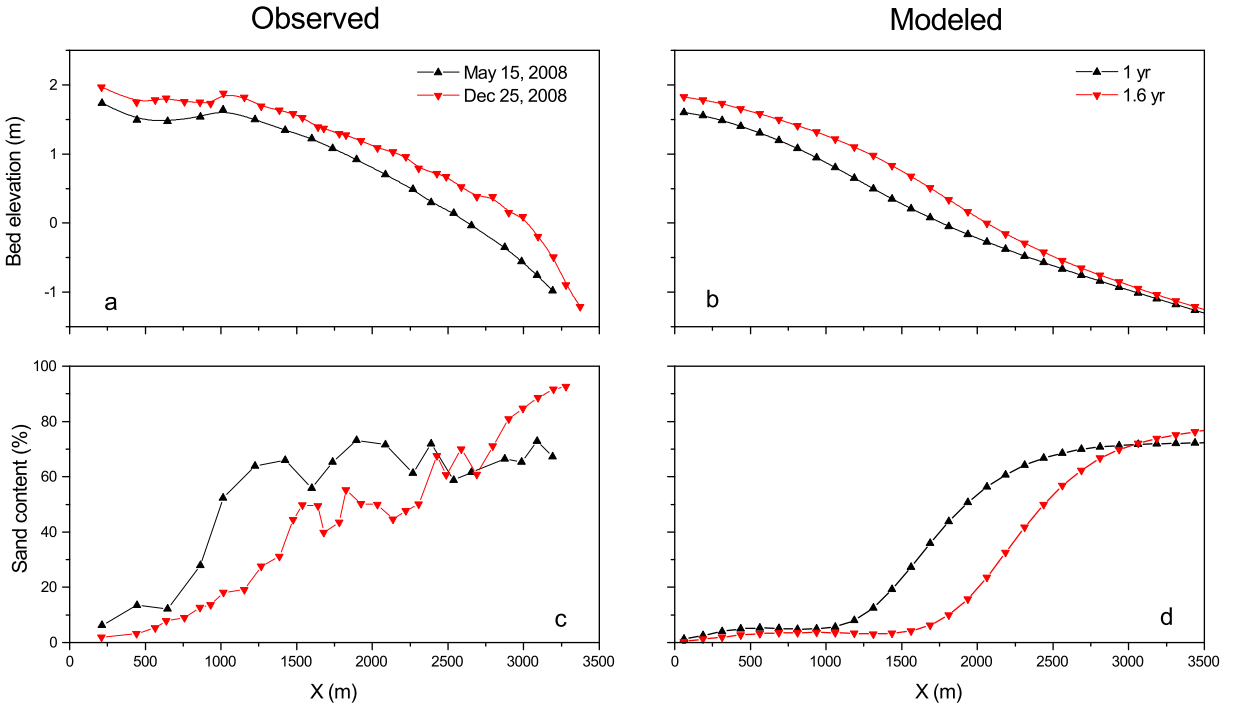
Observed
Modeled
May 15, 2008
Dec 25, 2008
1 yr
1.6 yr
Bed elevation (m)
Sand content (%)
X (m)
X (m)
a
b
c
d

Figure 5.

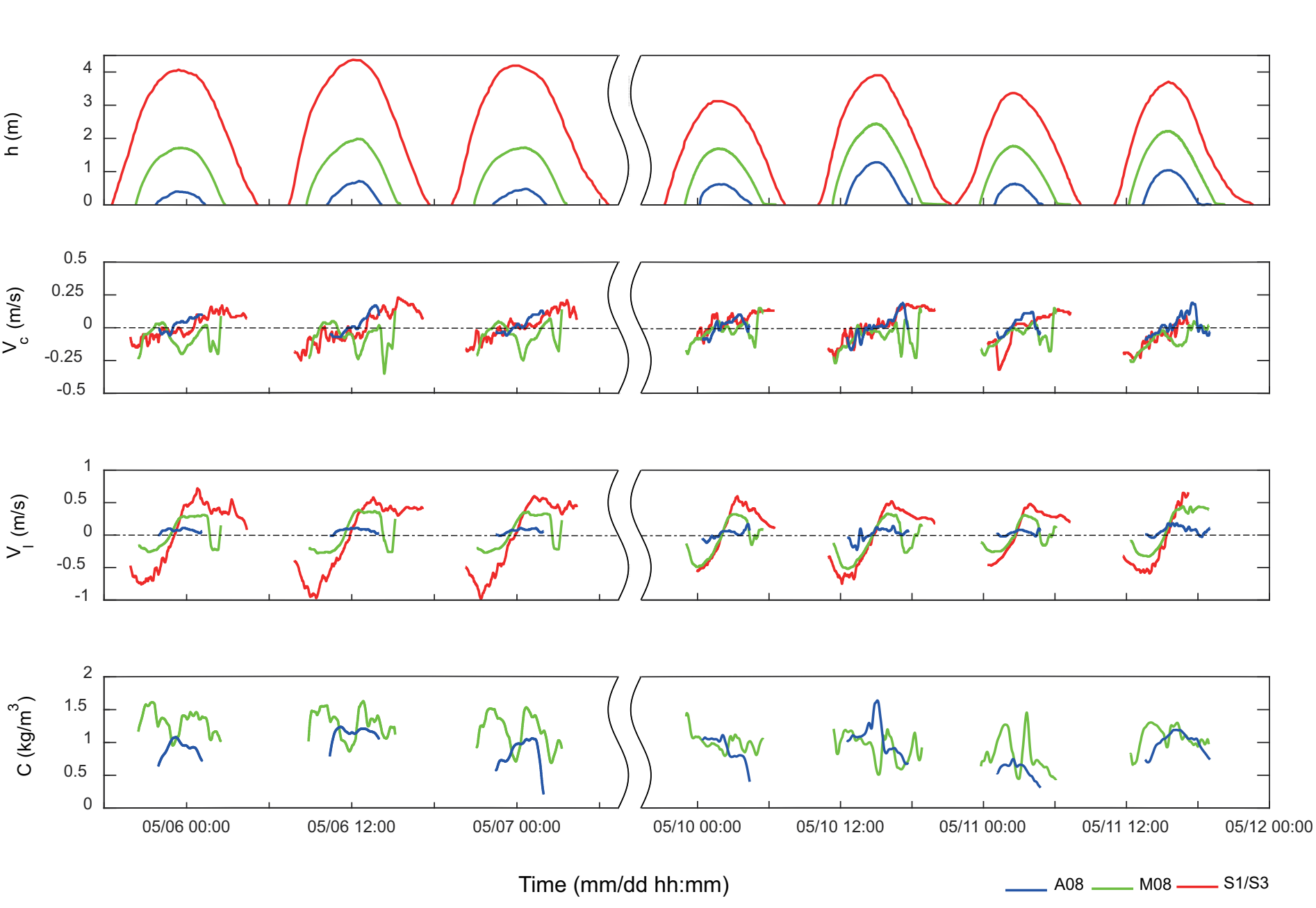
h (m)
4
3
2
1
0
V c (m/s)
0.5
0.25
0
-0.25
-0.5
V l (m/s)
1
0.5
0
-0.5
-1
C (kg/m 3)
2
1.5
1
0.5
0
05/06 00:00
05/06 12:00
05/07 00:00
05/10 00:00
05/10 12:00
05/11 00:00
05/11 12:00
05/12 00:00
Time (mm/dd hh:mm)
A08
M08
S1/S3

Figure 6.

a. initial
b. 2nd year
c. 4th year
d. 6th year
e. initial
f. 2nd year
g. 4th year
h. 6th year
y coordinate (km) →
x coordinate (km) →
Elevation (m)
Distance along cross-section (m)
Bed elevation (m)
Volume fraction of mud

Figure 7.

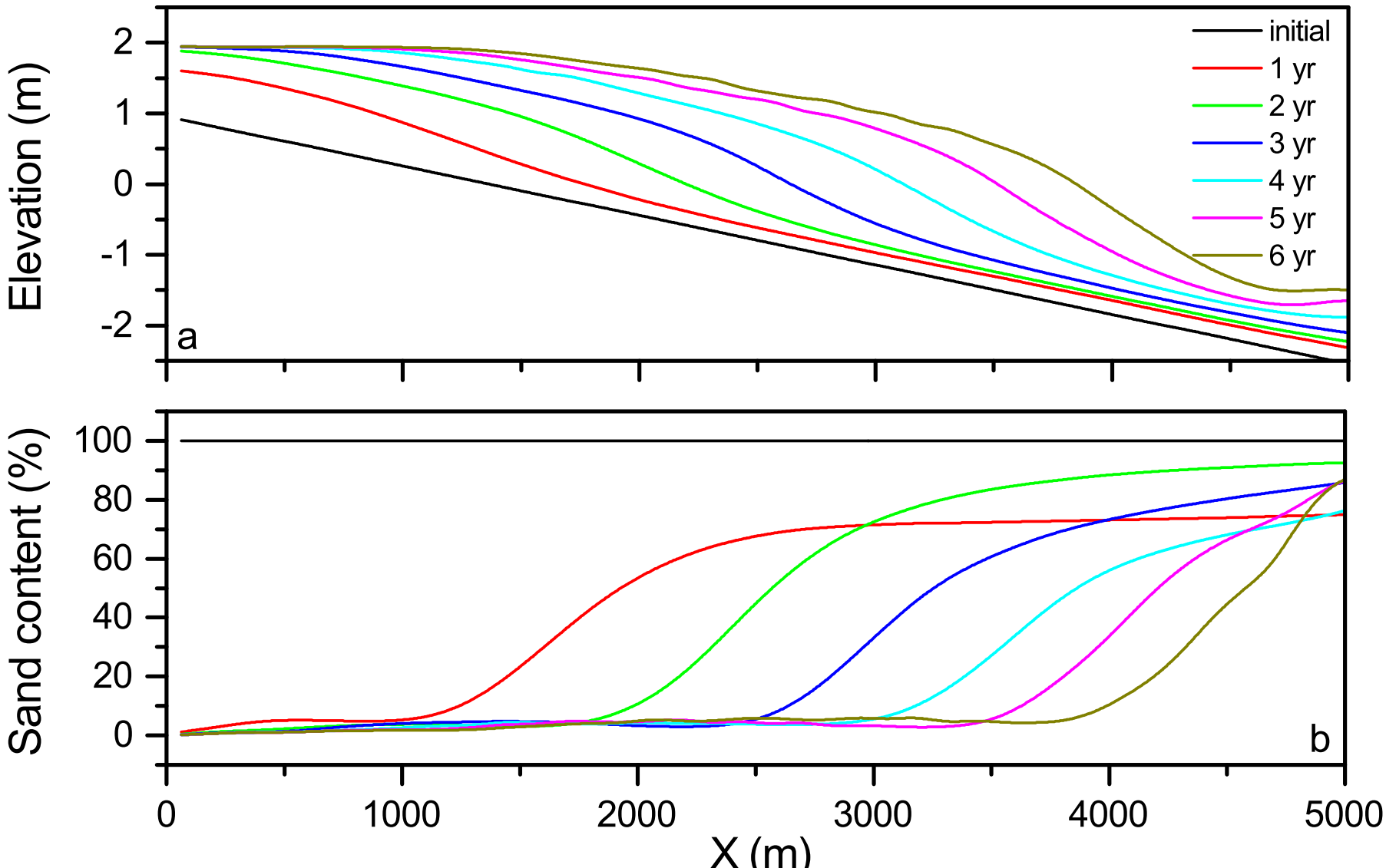
Elevation (m)
2
1
0
-1
-2
a
initial
1 yr
2 yr
3 yr
4 yr
5 yr
6 yr
Sand content (%)
100
80
60
40
20
0
b
0
1000
2000
3000
4000
5000
X (m)

Figure 8.

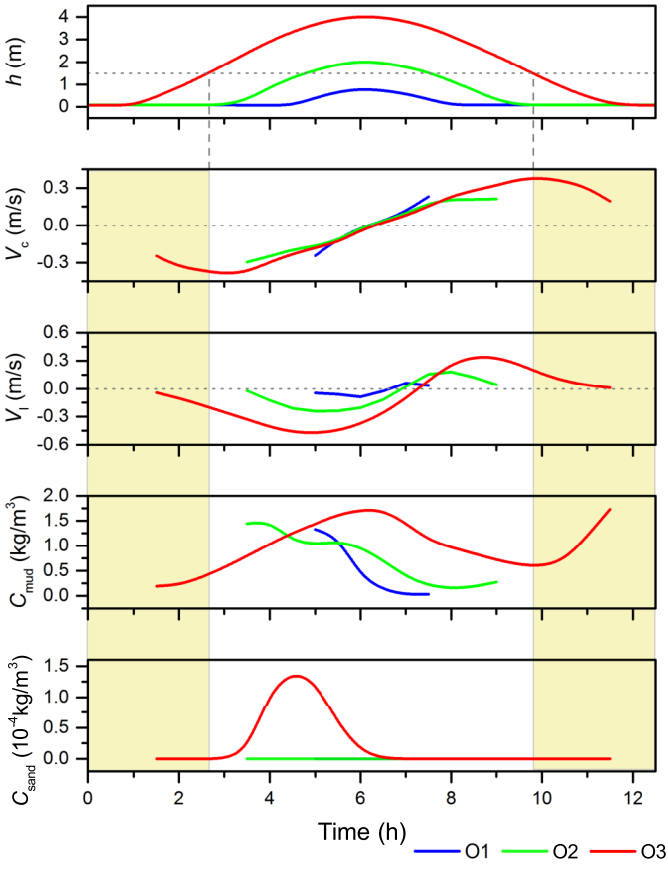
h (m)
4
3
2
1
0
V_c (m/s)
0.3
0.0
-0.3
V_l (m/s)
0.6
0.3
0.0
-0.3
-0.6
C_mud (kg/m^3)
2.0
1.5
1.0
0.5
0.0
C_sand (10^-4 kg/m^3)
1.5
1.0
0.5
0.0
0
2
4
6
8
10
12
Time (h)
O1
O2
O3

Figure 9.

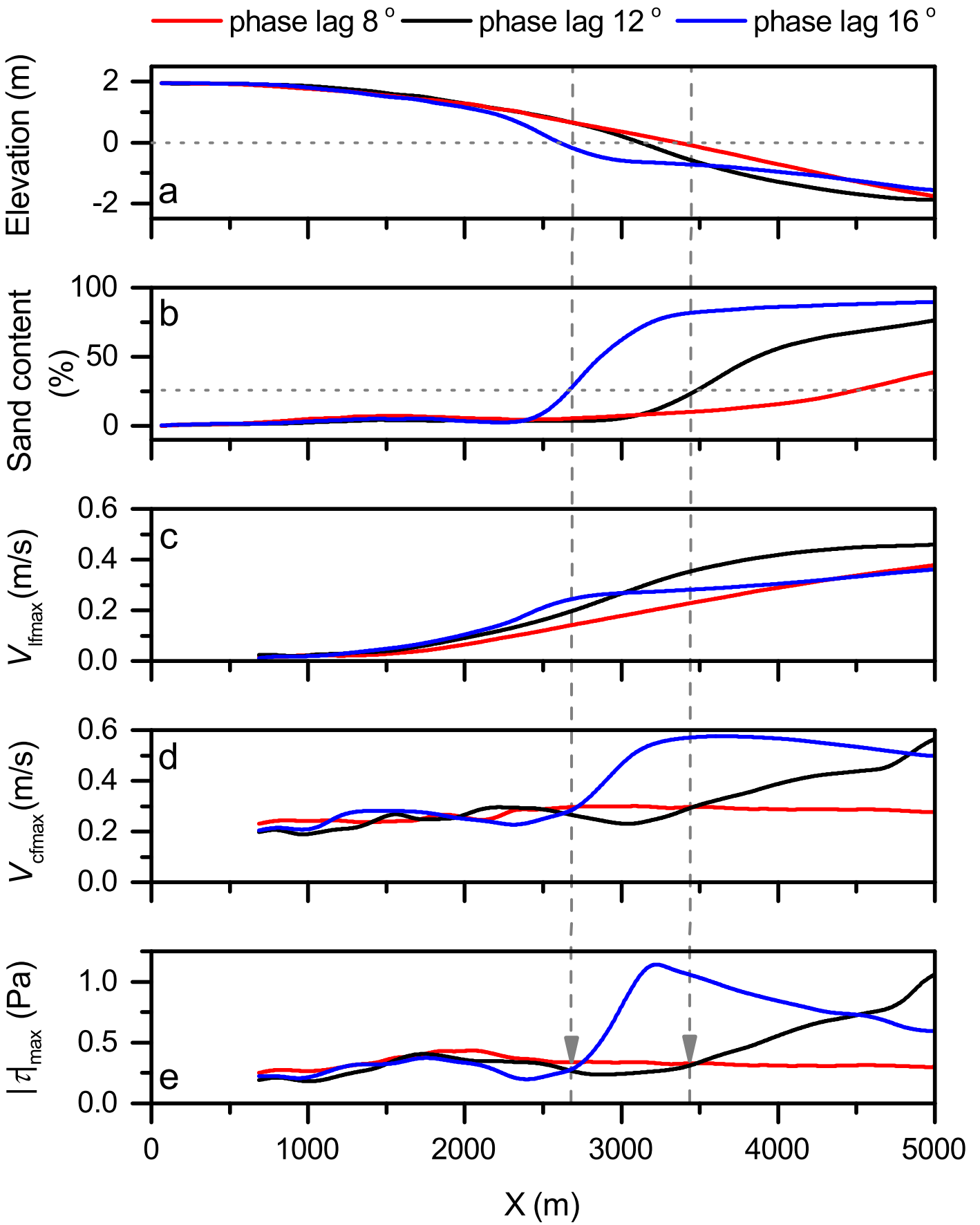
phase lag 8 °
phase lag 12 °
phase lag 16 °
Elevation (m)
2
0
-2
a
Sand content (%)
100
50
0
b
V_{lfmax} (m/s)
0.6
0.4
0.2
0.0
c
V_{cfmax} (m/s)
0.6
0.4
0.2
0.0
d
$|\tau|_{max}$ (Pa)
1.0
0.5
0.0
e
0
1000
2000
3000
4000
5000
X (m)

Figure 10.

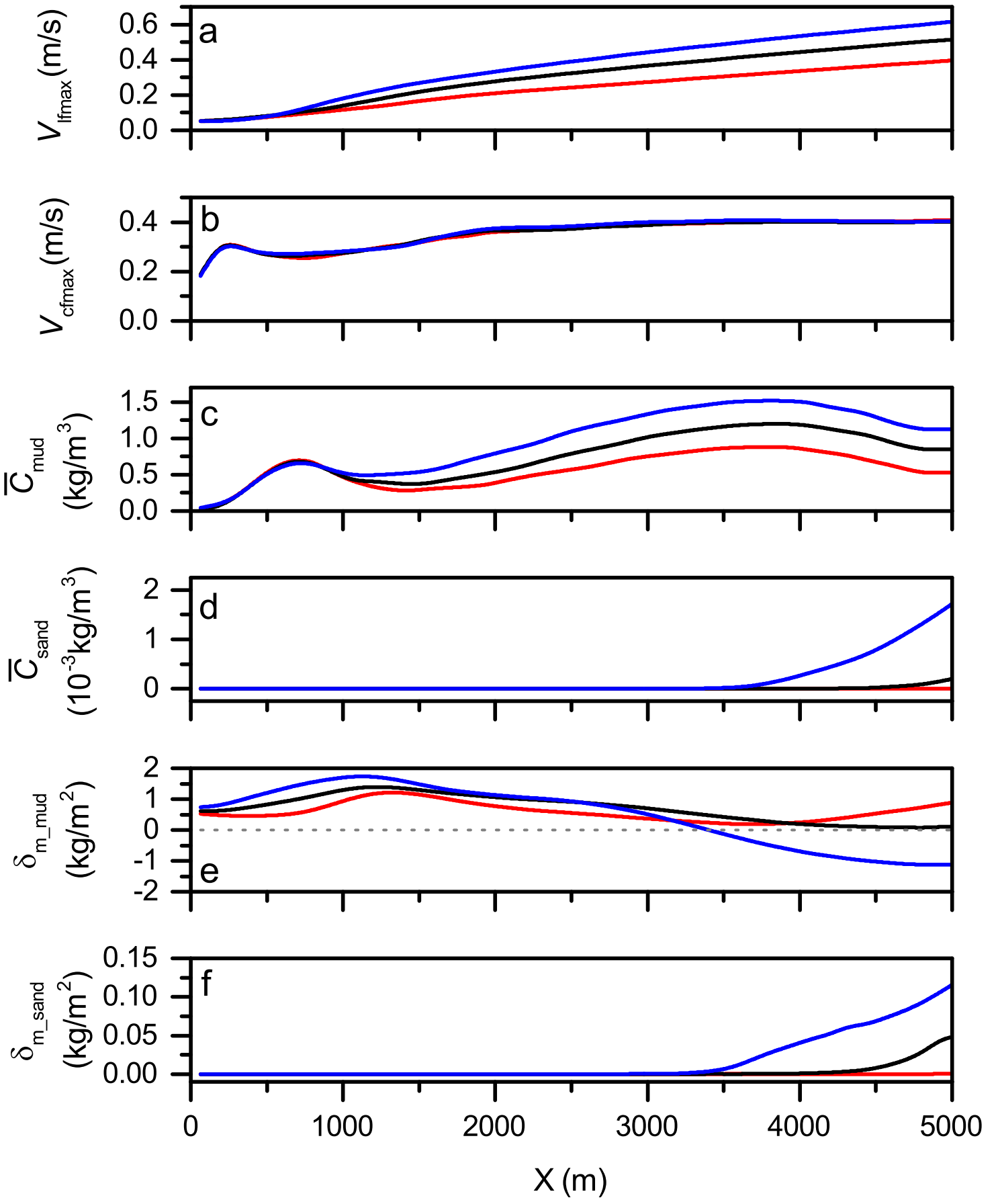
a
b
c
d
e
f
V_{lfmax} (m/s)
V_{cfmax} (m/s)
$\overline{C}_{mud}$ (kg/m^3)
$\overline{C}_{sand}$ (10^{-3}kg/m^3)
δ_{m_mud} (kg/m^2)
δ_{m_sand} (kg/m^2)
0.6
0.4
0.2
0.0
0.4
0.2
0.0
1.5
1.0
0.5
0.0
2
1
0
2
1
0
-1
-2
0.15
0.10
0.05
0.00
0
1000
2000
3000
4000
5000
X (m)
phase lag 8 °
phase lag 12 °
phase lag 16 °